Late Holocene covariability of the southern westerlies and sea surface temperature in northern Chilean Patagonia

Sébastien Bertrand [1,2,*] Konrad Hughen [1], Julio Sepúlveda [3,a], Silvio Pantoja [4]

[1] Marine Chemistry and Geochemistry, Woods Hole Oceanographic Institution, 360 Woods Hole Road, MA02543, Woods Hole, USA

[2] Renard Centre of Marine Geology, Ghent University, Krijgslaan 281 S8, 9000 Gent, Belgium

[3] Department of Earth, Atmospheric and Planetary Sciences, Massachusetts Institute of Technology, 45 Carleton Street, E25-623, MA02139, Cambridge, USA

[4] Department of Oceanography and Center for Oceanographic Research in the eastern South Pacific, University of Concepción, P.O. Box 160-C, Concepción, Chile

[a] Now at: Geological Sciences and Institute of Arctic and Alpine Research (INSTAAR), University of Colorado, Boulder, USA

[*]Corresponding author: sbertrand@whoi.edu, sebastien.bertrand@ugent.be

Abstract

The climate of Chilean Patagonia is strongly influenced by the southern westerlies, which control the amount and latitudinal distribution of precipitation in the southern Andes. In austral summer, the Southern Westerly Wind Belt (SWWB) is restricted to the high latitudes. It expands northward in winter, which results in a strong precipitation seasonality between ~35 and 45°S. Here, we present a new precipitation seasonality proxy record from Quitralco fjord (46°S), where relatively small latitudinal shifts in the SWWB result in large changes in precipitation seasonality. Our 1400 yr record is based on sedimentological and geochemical data obtained on a sediment core collected in front of a small river that drains the

Patagonian Andes, which makes this site particularly sensitive to changes in river discharge. Our results indicate Fe/Al and Ti/Al values that are low between 600 and 1200 CE, increasing at 1200–1500 CE, and high between 1500 and 1950 CE. Increasing Fe/Al and Ti/Al values reflect a decrease in mean sediment grain-size from 30 to 20 µm, which is interpreted as a decrease in seasonal floods resulting from an equatorward shift of the SWWB. Our results suggest that, compared to present-day conditions, the SWWB was located in a more poleward position before 1200 CE. It gradually shifted towards the equator in 1200–1500 CE, where it remained in a sustained position until 1950 CE. This pattern is consistent with most precipitation records from central and southern Chile. The comparison of our record with published regional sea surface temperature (SST) reconstructions for the late Holocene shows that equatorward shifts in the SWWB are systematically coeval with decreasing SSTs and vice versa, which resembles fluctuations over glacial-interglacial timescales. We argue that the synchronicity between SST and SWWB changes during the last 1400 years represents the response of the SWWB to temperature changes in the Southern Hemisphere.

Keywords

Southern westerlies, inorganic geochemistry, paleohydrology, paleohydroclimatology, fjord sediments, southern South America, Chilean Patagonia

1. Introduction

The southern westerlies are the prevailing winds at the mid latitudes of the Southern Hemisphere, blowing between the subtropical anticyclone and the cyclonic subpolar air masses. The Southern Westerly Wind Belt (SWWB) extends roughly between 30 and 60ºS, and it exhibits latitudinal variations at seasonal to glacial-interglacial timescales. Due to the

absence of continental barriers in the Southern Ocean, the SWWB directly controls the strength of the Antarctic Circumpolar Current (ACC), which in turn affects the release of CO_2 from the deep ocean up to the atmosphere, particularly on glacial-interglacial timescales (Anderson et al., 2009). In addition to modulating the strength of the ACC, the SWWB also controls the amount of precipitation on the windward side of the mountain ranges located along its path such as the southern Andes and the southern Alps of New Zealand. In western Patagonia, high westerly-driven precipitation supports extensive rainforests and large rivers, and it sustains the temperate glaciers that compose the Patagonian icefields and Darwin Cordillera (Masiokas et al., 2008; Garreaud et al., 2013). As a result, precipitation variability in the southwestern Andes is one of the most important factors that control Patagonian glacier mass balance at centennial to millennial timescales (Bertrand et al., 2012a; Boex et al., 2013). In the last decades, the SWWB has migrated poleward, causing a decrease in annual precipitation in southern Chile, which accelerated glacier retreat in Patagonia (e.g., Warren, 1993; Masiokas et al., 2008), increased desertification in northern Chile (e.g., Salinas and Mendieta, 2013), and reduced the amount of freshwater available for irrigation and consumption (Minetti et al., 2003; Meza, 2013). Given the impact that the SWWB has on global atmospheric CO_2 concentrations, and on the environment and socio-economic activities in South America, it is crucial to understand how its variations relate to changes in the global atmospheric and oceanic systems.

Southern Chile is ideally located to reconstruct past changes in the SWWB because it is the only continuous land mass that intersects the core and the entire northern half of the SWWB. In addition, due the orographic effect of the Andes, the SWWB almost entirely controls precipitation on the western side of the Andes. Paleohydrological records from

Chilean Patagonia therefore constitute one of the best ways to reconstruct past changes in the SWWB.

At glacial-interglacial timescales, the SWBB displays latitudinal variations of up to 10 degrees of latitude, which are closely related to global temperature changes (Toggweiler et al., 2006). The SWWB is generally located in an equatorward position under cold glacial conditions, and it shifts poleward during warm interglacials (Toggweiler et al 2006; Kohfeld et al., 2013; Lamy et al., 2014). This behavior differs from present-day seasonal variations, during which the SWWB does not significantly shifts latitudinally but rather shows a contraction in austral summer and an expansion in austral winter (Garreaud et al., 2009; Lamy et al., 2010). On intermediate timescales, high frequency changes in the SWWB are increasingly interpreted as reflecting variations in the Southern Annual Mode (SAM; e.g., Villalba et al., 2012; Moreno et al., 2014).

Although SWWB variability at seasonal (Garreaud et al., 2009, 2013) and glacial-interglacial (Kohfeld et al., 2013) timescales is relatively well understood, a lot of uncertainties remain regarding SWWB variations on centennial timescales during the Holocene (e.g., Kilian and Lamy, 2012). For more than a decade, authors have discussed Holocene SWWB variability using proxy evidence from single sites located along the path of the SWWB in southern South America (e.g., Lamy et al., 2001; Jenny et al., 2002; Bertrand et al., 2005; Villa-Martinez and Moreno, 2007; Moreno et al., 2009; Sepúlveda et al., 2009). Variations in the amount of precipitation were generally interpreted as representing either latitudinal shifts or weakening/strengthening of the entire wind belt. More recently, authors have tried to refine the Holocene evolution of the SWWB in southern South America by comparing precipitation records located within the present-day core of the SWWB to records located at the northern limit of the wind belt. This approach has however led to different conclusions,

98 with Moreno et al. (2010) arguing for a weakening of the entire SWWB during the early
99 Holocene, and Lamy et al. (2010) proposing an expansion/contraction mechanism to
100 resemble present-day seasonal variations.
101 Here, we reconstruct SWWB variability during the late Holocene using a different approach.
102 We take advantage of the modern distribution in precipitation seasonality in the southern
103 Andes to reconstruct variations in the latitudinal position of the SWWB. Because of the
104 strong contrast between precipitation regimes immediately to the north (strong
105 precipitation seasonality) and to the south (year-round precipitation) of our study site at
106 46ºS, relatively small latitudinal shifts of the SWWB in either direction result in large changes
107 in precipitation seasonality. More specifically, we use inorganic geochemical measurements
108 obtained on a sediment core from Quitralco fjord to reconstruct past changes in regional
109 hydrology. We focus on Al, Ti, and Fe, since data on surface samples from the fjords of
110 Northern Chilean Patagonia show that these elements are ideally suited to reconstruct past
111 changes in hydrodynamics, i.e. in the intensity of river discharge, which is directly linked to
112 precipitation in the Andes (Bertrand et al., 2012b). We then compare our precipitation
113 seasonality record to regional sea surface temperature (SST) reconstructions to assess the
114 ocean-atmosphere linkages in Patagonia during the last 1400 years.
115
116 **2. Regional settings**
117 2.1 Climate
118 The climate of Northern Chilean Patagonia (~40–48ºS) is clearly oceanic, temperate and
119 hyperhumid, with freezing levels generally above 1 km a.s.l. (Garreaud et al., 2013). In this
120 area, precipitation ranges from >3000 mm/yr on the western side of the Andes to less than
121 600 mm/yr at the border with Argentina (Fig. 1). Precipitation on the windward (western)

side of the Patagonian Andes is almost entirely controlled by the SWWB and the orographic effect of the Andes (Garreaud et al., 2013). In the ocean-dominated Southern Hemisphere, the latitudinal position and strength of the SWWB is in turn mostly controlled by gradients in temperature over the Pacific and Southern Oceans, which influence the strength of the high-pressure areas of the subtropics (southeast Pacific anticyclone) and the low-pressure areas that prevail over the poles. Thus, a strong 'blocking' Pacific anticyclone can deflect the SWWB southwards, whereas high-latitude cooling and increased sea-ice around Antarctica can push the SWWB towards the equator (Bentley et al., 2009).

The present-day core of the SWWB is located at 52–53ºS (Fig. 2). It shows very limited latitudinal variations with seasons, with a southerly position (~55ºS) in winter when the wind belt expands, and a northerly position (~50ºS) in summer when it contracts (Fig. 2; Garreaud et al., 2009). In austral summer (DJF), the SWWB contracts and the zonal wind speed increases (Fig. 2a). In winter (JJA), the SWWB expands in both directions and wind speed decreases (Fig. 2b, c). As a result, the region between 35 and 45ºS is characterized by a strong precipitation seasonality, with relatively dry summers and wet winters (Fig. 1b). The duration of the dry summer season decreases southwards (see animation in Appendix 1).

In the Quitralco fjord area (46ºS), the climate is characterized by long but relatively mild winters (winter mean temperature: 4ºC) and cool and short summers (summer mean temperature: 13ºC). The modern snowline is located at ~2000 m, and snow only occurs a few days per year at sea level (Miller, 1976). The precipitation regime at Quitralco fjord is best represented by the meteorological station at Puerto Chacabuco, which is located 60 km to the NE of Quitralco fjord (Fig. 1a). At Puerto Chacabuco, annual precipitation reaches 2929 mm, and the precipitation regime is weakly seasonal, with 305 mm/month in winter (JJA) and 188 mm/month in summer (DJF). Large precipitation events, with precipitation

146 rates of up to 98 mm/24 hours occur mostly in fall and winter. By comparison, the Puerto
147 Marin station, which is located about 2º of latitude to the North (Fig. 1a), displays similar
148 annual precipitation values (3082 mm), but a more pronounced seasonal signal, with winter
149 precipitation (366 mm/month) being twice as high as precipitation in the summer months
150 (167 mm/month). On the contrary, precipitation at Isla San Pedro, about 2º of latitude to the
151 South, shows high year-round precipitation and a lack of seasonal variability (Fig. 1a).
152 Precipitation at Puerto Chacabuco is also strongly correlated with zonal wind speed
153 (Garreaud et al., 2013, Appendix 2). A poleward shift of the SWWB would therefore not
154 significantly affect annual precipitation amounts in the Quitralco area, but it would result in
155 a significant increase in precipitation seasonality, providing a precipitation regime similar to
156 the current situation at Puerto Marin (Fig. 1a). An equatorward shift, on the other hand,
157 would cause a decrease in precipitation seasonality.
158 In the last decades, global warming and the increasing ozone hole over Antarctica have
159 caused an increase in temperature difference between the Southern Hemisphere mid- and
160 high-latitudes, resulting in a poleward shift and contraction of the SWWB, which in turn
161 caused a strengthening of westerly wind speeds over the Southern Ocean (Shindell and
162 Schmidt, 2004; Toggweiler, 2009; Sen Gupta et al., 2009; Thompson et al., 2011; Garreaud et
163 al., 2013). This recent poleward shift of the SWWB, which represents a positive phase of the
164 SAM (Thompson et al., 2011), has caused a general decrease in annual precipitation in
165 central and southern Chile between 35 and 50ºS (Aravena and Luckman, 2009; Quintana and
166 Aceituno, 2006, 2012). This trend, which is particularly marked between 37 and 43ºS since
167 1950 (Quintana and Aceituno, 2012), is mostly due to a reduction in summer precipitation,
168 resulting in an increase in precipitation seasonality over northern Chilean Patagonia.
169 Between 1980 and 2010, precipitation seasonality on the western coast of northern Chilean

Patagonia (41–48ºS) has increased on average by 19% (Appendix 3). Projections for the 21st century (Vera et al., 2006; Meehl et al., 2007; Appendix 4) indicate a continued decrease in annual precipitation over northern Chilean Patagonia, which is more pronounced in summer than in winter, resulting in a further increase in precipitation seasonality.

2.2 Oceanography

The large-scale surface circulation off southernmost Chile is dominated by the ACC, the world's largest current system (Mayewski et al., 2009), which flows uninterrupted and clockwise around Antarctica. The strength of the ACC largely depends on the latitudinal position and intensity of the SWWB. The northern part of the ACC reaches the coast of southern Chile, where it splits into two coastal branches: the Cape Horn current to the South and the Humboldt, or Peru-Chile, current to the North (Fig. 1a). The Antarctic water mass flows inwards in most of the fjords between ~30 m and ~150 m depth (Silva and Guzman, 2006; Sievers and Silva, 2008). It is overlain by a surface estuarine water mass (Chilean Fjord Water, CFW), which flows out of the fjords towards the Pacific Ocean between 0 and ~30 m depth. The extension and depth of the CFW depends on the amount of freshwater supplied by rivers, glaciers, coastal runoff and direct precipitation. Along the coast of Chilean Patagonia, SST in the eastern South Pacific shows a gradual decrease poleward, with a gradient of ~0.5ºC per degree of latitude (Fig. 1). The gradient is more pronounced in summer, when the zonal systems contract.

Quitralco fjord is one of the SW-NE oriented fjords that form the fjord region of Northern Chilean Patagonia (Fig. 3). It is composed of a main ~15 km long basin that has accumulated sediment continuously throughout the Holocene (Araya-Vergara, 1997, Vieira, 2002). The bottom of the basin is slightly concave with depths between 100 and 125 m (Vieira, 2002;

194 SHOA, 2004). Quitralco fjord has no major river inflow at its head but it receives significant
195 amounts of freshwater through Rio Pelu, which drains its southern flank (Fig. 3).
196
197 2.3 Geology
198 The watershed of Rio Pelu belongs to the North Patagonian Batholith, which is composed of
199 Cenozoic and Mesozoic granitoids (Pankhurst et al., 1999; Sernageomin, 2003). Around
200 Quitralco fjord the batholith is dominated by hornblende-biotite tonalite (Pankhurst et al.,
201 1999). In addition, Quitralco fjord is located near three of the thirteen Quaternary volcanoes
202 that compose the southern segment of the southern volcanic zone (SSVZ, 42–46°S):
203 volcanoes Cay, Macá and Hudson, the latter being by far the most active (Stern et al., 2007).
204 Due to the prevailing westerly winds and the location of Quitralco fjord to the NW of Hudson
205 volcano, the region is only slightly affected by the eruptive products (e.g., Naranjo and Stern
206 1998). The regional soil cover is dominated by thin andosols, i.e., soils developed on the
207 Holocene volcanic ashes that reached the area (Gut, 2008; Vandekerkhove, 2014).
208
209 2.4 Morphology and vegetation
210 The watershed of Rio Pelu has a surface area of 138.7 km^2, with elevations ranging from 0 to
211 1589 m. The slopes within the watershed are steep, with an average of 19 degrees. Most of
212 the watershed is presently covered by a dense temperate evergreen forest (Fig. 3) mostly
213 composed of *Nothofagus betuloides* and *Desfontainia spinosa* (Luebert and Pliscoff, 2006),
214 reflecting the high year-round precipitation in the area. Less than 2% of the watershed is
215 covered by glaciers (Fig. 3). River discharge is therefore mostly controlled by rainfall.
216
217 **3. Material and methods**

218 3.1 Coring and sediment sampling

219 Sediment core PC29A (45.756°S – 73.467°W) was collected at a depth of 112 m in Quitralco
220 fjord during the CIMAR (Cruceros de Investigación Marina) Fiordos 7 expedition (CF7) in
221 November 2001, aboard R/V AGOR Vidal Gormáz. The coring site is located immediately in
222 front of Rio Pelu (Fig. 3). It is therefore particularly sensitive to changes in river discharge.
223 The 208 cm long piston core was split lengthwise and described at the Woods Hole
224 Oceanographic Institution, MA, USA, where it was subsequently stored at 4°C. A complete
225 core half was sub-sampled in 1 cm thick slices, which were immediately freeze-dried and
226 ground using an agate mortar. Wet and dry sample weights were recorded for water content
227 calculation. The archive half was used for XRF core scanning. Additionally, small (~0.1 cc)
228 samples were taken every 4 cm in the archive half for grain size analysis, and preserved wet
229 in microcentrifuge tubes. Shell and leaf/wood remains were collected from both core halves
230 for radiocarbon dating. These samples were cleaned with milli-Q water under a binocular
231 lens and sent to NOSAMS for analysis. A box core (BC29A) was also collected at the same
232 site, and sub-sampled on board in 1 cm thick slices.
233
234 3.2 Age model
235 The chronology of sediment core PC29A is based on seven AMS radiocarbon ages obtained
236 on organic (n=5) and inorganic (n=2) macro-remains picked in the sediment core (Table 1).
237 Although the upper 50 cm of the archive half was entirely sieved, no terrestrial macro-
238 remain was found in that part of the core. Radiocarbon ages were calibrated with CLAM 2.2
239 (Blaauw, 2010), using the calibration curve SHCal13 (Hogg et al., 2013). The reservoir age
240 correction commonly used for the eastern South Pacific (530 years; Mohtadi et al., 2007)
241 was applied to the two mollusk samples. In addition, a comparison between the upper part

242 of PC29A piston core with the box core using $\delta^{13}C$ values (Appendix 5) demonstrated that no
243 sediment had been lost during the coring operation. We therefore attributed an age of 2001
244 to the sediment-water interface. The final age model was generated using CLAM 2.2.
245
246 3.3 Inorganic geochemistry
247 Sediment core PC29A was scanned on an ITRAX XRF core scanner (Cox Analytical
248 Instruments) at a resolution of 1 mm. The scanner was operated with 20 sec scan times
249 using a Mo X-Ray tube set to 30 kV and 45 mA. The XRF spectra were interpreted and the
250 peak areas quantified using the Q-Spec 6.5 software.
251 A subset of 102 samples from core PC29A was analyzed for inorganic geochemistry by ICP-
252 AES. Samples were prepared using the Li-metaborate (LiBr) fusion technique of Murray et al.
253 (2000), which is preferred over HF digestion because it is the only technique that allows the
254 complete dissolution of sediment samples containing refractory minerals such as zircon
255 (Huang et al., 2007). Sample preparation consisted in mixing 50±0.5 mg of sediment with
256 200±1.0 mg of ultrapure Li-metaborate (SCP Science) in 3ml Pt:Au (95:5) crucibles. Ten µl of
257 25% LiBr were then added to the mixture and the crucibles were placed in a muffle furnace
258 for 12 minutes at 1050°C. The newly formed glass beads were then allowed to cool down for
259 2–3 min, detached from the crucible, and poured into a Teflon beaker containing a swirling
260 25 ml solution of 5% HNO_3. Complete dissolution occurred within ~30 min. The solution was
261 then filtered through a 0.45 µm PVDF Millipore filter and diluted in 5% HNO_3 to obtain a
262 4000 x final dilution of the sample. The exact dilution factor was calculated from the precise
263 weight of sediment used for fusion.
264 Thirteen elements were measured on a JY Ultima C ICP-AES. Analytical details are given in
265 Bertrand et al. (2012b). Here, we focus on the lithophile and mostly immobile elements Fe,

Ti, and Al, to reconstruct changes in hydrodynamic conditions following Bertrand et al. (2012b), as well as Si. Analytical precision (1 σ), which was calculated from the analysis of ten individually-prepared sub-samples of reference sediment PACS-2, is 0.66 % for Al, 0.71 % for Fe, 1.03% for Ti, and 0.68 % for Si. Precision for the elemental ratios Fe/Al and Ti/Al is 0.66 % and 0.68 %, respectively.

3.4 Mineralogy

The bulk mineralogy of the same 102 samples was analyzed by X-ray diffraction (XRD) on a Bruker D8-Advance diffractometer with CuKα radiation. Samples were mounted as unoriented powder using the back-side method (Brindley and Brown, 1980), and subsequently scanned by XRD between 2° and 45° 2θ. Peak intensities were used to quantify (± 5 wt. %) the mineral proportions, following Cook et al. (1975). Clay minerals were not identified or quantified on the bulk diffractograms. Although halite was detected in all the sediment samples, it was not quantified because it derives from interstitial water salts that precipitated during freeze-drying.

3.5 Bulk organic geochemistry

Approximately 50 mg of ground sediment was weighed in tin capsules and treated with 1N sulphurous acid to remove eventual carbonates (Verardo et al., 1990). Total Organic Carbon (TOC), Total Nitrogen (TN) and stable isotope ratios of carbon ($\delta^{13}C$) were measured at the UCDavis Stable Isotope Facility by continuous flow isotope ratio mass spectrometry (CF-IRMS; 20-20 SERCON mass spectrometer) after sample combustion to CO_2 and N_2 at 1000°C in an on-line elemental analyzer (PDZEuropa ANCA-GSL). The precision, calculated by replicate analysis of the internal standard, is 0.04 ‰ for $\delta^{13}C$.

290

291 3.6 Carbonate content

292 The weight percentage of total inorganic carbon (TIC) in bulk sediment samples was
293 determined every 5 cm using an UIC CM5014 coulometer equipped with a CM5130
294 acidification module. For each sample, 50–60 mg of sediment was precisely weighed in a 4ml
295 glass vial and treated with 1.5 ml 1N H_3PO_4 to liberate CO_2. The percentage of carbonate was
296 calculated from the TIC data using the following equation: $CaCO_3$ (wt%) = TIC (wt%) x 8.33,
297 assuming that 100% of the measured CO_2 is derived from dissolution of calcium carbonate.
298 The analytical precision, determined from 7 entirely separate analyses of a sediment sample
299 from site PC29A, was 0.04% $CaCO_3$.

300

301 3.7 Biogenic opal

302 Biogenic silica (bio-Si) was analyzed according to Carter and Colman (1994) and Mortlock and
303 Froelich (1989). Samples were extracted with NaOH after removal of organic matter and
304 carbonate with 10% H_2O_2 and 1N HCl, respectively. They were subsequently diluted in 5%
305 nitric acid and analyzed in triplicate for Si and Fe on a JY Ultima-C ICP-AES. Al was measured
306 in triplicate by flame atomic absorption spectrometry (FAAS) on a Varian SpectrAA 220.
307 Measured Si concentrations were corrected for detrital Si using the measured Al
308 concentrations: bio-Si = measured Si – 2 x Al. The 2:1 ratio accounts for Si leached from
309 volcanic glasses and clay minerals. This correction assumes that all Al originates from the
310 dissolution of detrital particles. The precision on bio-Si, determined from 5 entirely separate
311 analyses of a sediment sample from site PC29A, was 0.46 %. Biogenic opal (bio-opal, $SiO_2 \cdot nH_2O$, wt. %) was obtained by multiplying the bio-Si values by 2.4 (Mortlock and Froelich,

1989). Lithogenic silica (litho-Si, wt. %) was calculated by difference (Total Si [see 3.3] – bio-Si).

3.8 Grain-size

Grain-size was measured on the terrigenous fraction of the sediment using a Coulter LS200 laser grain-size analyzer. The terrigenous fraction was isolated by treating the samples with boiling H_2O_2, HCl and NaOH, to remove organic matter, carbonates and biogenic silica, respectively. Prior to analysis, samples were boiled with 300 mg of sodium pyrophosphate ($Na_4P_2O_7 \cdot 10H_2O$) to ensure complete disaggregation of the particles. The grain-size distribution of the samples was measured during 90 seconds and the arithmetic mean was calculated from the 92 size classes. Downcore grain-size distributions were unmixed using the end-member modeling algorithm of Weltje and Prins (2007).

4. Results

4.1 Lithology

Sediment core PC29A is composed of grayish olive (5Y 4/2) homogenous mud. No sedimentary structures or tephra layers were visible macroscopically but abundant small organic matter debris was observed between 208 and 169 cm. The sediment is composed of lithogenic particles (84.0 ± 0.7 wt. %; calculated as 100% – bio-opal – 2.2 x TOC – $CaCO_3$; Bertrand et al., 2012b), biogenic opal (13.2 ± 0.8 wt. %), organic matter (2.78 ± 0.36 wt. %; calculated as 2.2 x TOC), and very little carbonate (0.05 ± 0.03 wt. %) (average ± 1 s.d). Downcore plots (Fig. 4) clearly show a continuous increase in biogenic opal towards the top of the core and a modest decrease in TOC in the upper 65 cm, resulting in only very minor

variations in the lithogenic content of the sediment (Fig. 4). According to the $\delta^{13}C$ values, roughly half of the organic carbon is of terrestrial origin (Appendix 5).

4.2 Chronology

The final CLAM age model of core PC29A consists in a smooth spline (smooth factor 0.35) fitting through the probability distributions of the calibrated radiocarbon ages (Fig. 5). A smooth spline is preferred over linear regressions since there are no visible features in the sediment core that indicate abrupt changes in accumulation rates. The bottom of the core (208 cm) is dated at 605 CE (95% confidence interval: 556–656 CE). Accumulation rates range from 3.7 mm/yr at the bottom of the core to 0.6 mm/yr in the upper centimeter.

4.3 Inorganic geochemistry

The XRF core scanner data show significant increases in Fe and Ti in the upper ~50 cm of the sediment core, with a return to lower values in the top 23 mm (Fig. 6). The ICP-AES measurements show very similar trends for both elements, resulting in high correlations between XRF and ICP measurements ($r=0.85$, $p<0.001$ for Fe and $r=0.92$, $p<0.001$ for Ti). Al concentrations are mostly constant throughout the core (7.80 ± 0.13 wt. %), reflecting the constant lithogenic content of the sediment (Fig. 4). Fe and Ti XRF counts are therefore also highly correlated to Fe/Al ($r=0.88$, $p<0.001$) and Ti/Al ($r=0.93$, $p<0.001$).

4.4 Grain-size and mineralogy

The grain-size of the terrigenous fraction of the sediment shows high values in the lowermost part of the core (average of 29.8 µm below 168 cm), slightly lower values between 168 and 60 cm (average: 27.2 µm), and then a constant decrease down to 17.4 µm

360 towards the top (Fig. 6). Most of the grain-size distribution plots are bimodal, with a fine
361 mode at 5.6 μm and a coarse mode at 30 μm (Appendix 6). A two end-member model, which
362 explains 67% of the variance of the total set of grain-size distributions, was therefore
363 selected. Both end-members co-exist in most of the core but the coarse end-member is
364 heavily reduced in the upper part of the core (Appendix 6).
365 The bulk mineralogical composition of sediment core PC29A (average ± 1 s.d.) is dominated
366 by plagioclase (43 ± 6%), K-feldspar (19 ± 4%), amphibole (14 ± 3 %), pyroxene (11 ± 3 %) and
367 quartz (10 ± 3 %), reflecting a mixture of volcanic (andosol) and granodioritic sources. The
368 quartz content of the sediment is high and rather constant below 52 cm (12 ± 3 %), and
369 much lower (7 ± 2 %) above (Fig. 6). Both grain-size and quartz display significant positive
370 correlations with litho-Si/Al ($r=0.82$, $p<0.01$ and $r=0.55$, $p=0.01$, respectively).
371
372 **5. Interpretation and discussion**
373 5.1 Controls on sediment composition
374 In modern sediments from the fjords of Northern Chilean Patagonia, Al concentrations
375 faithfully reflect the proportion of lithogenic particles in the sediment. Because Al is a
376 primary constituent of most aluminosilicate minerals, Al concentrations in the lithogenic
377 fractions of Chilean fjord sediments are mostly independent of changes in mineralogy and/or
378 grain-size (Bertrand et al., 2012b). This statement also applies to sediment core PC29A,
379 which shows very little downcore variations in the lithogenic content of the sediment (Fig. 4)
380 and Al concentrations (Fig. 6). Al concentrations in the lithogenic fraction of the sediment
381 are 9.33 ± 0.18%, in agreement with a mixture of granodioritic bedrock (8.16 ± 1.16%) and
382 volcanic ash soil (10.45 ± 1.50%) sources (Bertrand et al., 2012b). Al is therefore the ideal

383 lithogenic geochemical element to normalize other geochemical elements to in order to
384 assess changes in the lithogenic fraction of the sediment.
385 Since Al concentrations in core PC29A are roughly constant downcore, variations in the
386 concentrations of other lithogenic elements, such as the Fe and Ti (Fig. 6), mostly reflect
387 variations in the composition of the lithogenic fraction of the sediment and are not due
388 dilution by other sediment components. This is confirmed by the downcore trends in Fe/Al
389 and Ti/Al, which are highly positively correlated to the Fe and Ti XRF core scanner counts
390 (Fig. 6).
391 In sediment records from terrestrial and near-shore environments, increases in lithogenic
392 elements Fe and Ti are commonly interpreted as increases in terrestrial supply, which are in
393 turn interpreted as increased precipitation (e.g., Haug et al., 2001; Lamy et al., 2004).
394 Following this classical interpretation, the upper part of sediment core PC29A would be
395 interpreted as representing a higher terrestrial supply of particles, and therefore more
396 precipitation. However, the same upper part of the sediment core shows a significant
397 decrease in grain-size, reflecting a decrease in the energy of river discharge. This decrease in
398 grain-size is also supported by the decrease in quartz and litho-Si/Al, since quartz is always
399 enriched in the coarse fraction of North Patagonian fjord sediments (Bertrand et al, 2012b).
400 Increases in Fe and Ti therefore represent a decrease in hydrodynamic conditions, in
401 agreement with the data obtained on river-proximal fjord surface sediment samples
402 (Bertrand et al., 2012b). In these environments, increasing hydrodynamic conditions are
403 recorded as higher concentrations of coarse and refractory minerals, such as quartz, which
404 dilute Fe and Ti-bearing minerals, and are ultimately represented by the decrease of Fe and
405 Ti concentrations (Bertrand et al., 2012b). Although Fe variations alone could be attributed
406 to redox changes in the sediment, Ti is insensitive to environmental redox variations. The

407 excellent match between Fe and Ti concentrations in core PC29A ($r=0.98$, $p<0.0001$)
408 provides evidence that these elements are not controlled by diagenetic processes and that
409 either element reflects changes in the composition of the lithogenic fraction of the
410 sediment. In core PC29A, grain-size is therefore the single most important parameter that
411 controls downcore variations in mineralogy and inorganic geochemistry (lithogenic
412 elements).
413
414 5.2 Paleohydrological interpretation
415 The sediment deposited at coring site PC29A mostly originates from the settling of particles
416 transported in suspension in Rio Pelu (Fig. 3). Numerous processes can affect the particle
417 size distribution of suspended sediments in river systems (Walling and Moorehead, 1989;
418 Walling et al., 2000). For small mountain rivers, it appears that the size of particles
419 transported in suspension is mostly driven by changes in river discharge, and can therefore
420 be used to reconstruct flood intensity (Reid and Frostick, 1994; Lenzi and Marchi, 2000;
421 Grangeon et al., 2012). As a result sediment records in river-proximal environments, mostly
422 lakes, are frequently used to reconstruct the intensity of past flood events (Campbell, 1998),
423 which are in turn interpreted in terms of rainfall intensity / storminess (Noren et al., 2002;
424 Parris et al., 2010; Giguet-Covex et al., 2012) or snow melt intensity (nival freshet; Kaufman
425 et al., 2011).
426 Additional studies highlight the importance of precipitation seasonality in controlling the
427 grain-size and yield of suspended sediment in modern river systems because (1) vegetation
428 density, and therefore soil stability, decreases with increasing precipitation seasonality; (2)
429 intense rainfall results in more runoff than continuous rainfall because of the limited time
430 for water infiltration; and (3) the rate of soil erosion increases exponentially with runoff

(Milliman, 1997; Hooke, 2000; Guerra and Soares Da Silva 2011). This is also in agreement with Kaufman et al. (2011), who demonstrated that the grain-size of river-proximal lake sediments is strongly correlated to maximum spring daily discharge, and not to annual discharge.

Following these considerations, we interpret increases in sediment grain-size, and therefore decreasing Fe and Ti concentrations, at site PC29A as representing more intense seasonal floods of Rio Pelu, which are in turn interpreted as increased precipitation seasonality. The steep slopes that characterize the watershed of Rio Pelu make it particularly susceptible to soil erosion, and therefore sensitive to changes in precipitation seasonality. Although floods can also be triggered by rapid snow and/or ice melt, we believe that this process is negligible in the region of Quitralco fjord because (1) less than 3% of the watershed of Rio Pelu is currently covered by glaciers, and (2) the oceanic climate favors rainfall over snowfall. It must also have remained negligible during the last 1400 years, as indicated by the lack of glacigenic characteristics of the sediment throughout the core (Appendix 5). It should also be noted that there is no evidence of recent or past anthropogenic activities in the watershed of Rio Pelu. Soil erosion therefore only reflects natural processes.

With this in mind, downcore changes in Fe/Al, Ti/Al and grain-size (Fig. 6) can be interpreted in terms of changes in precipitation seasonality in Northern Chilean Patagonia. The record can be sub-divided in three major periods (Fig. 6): 600–1200 CE, which is characterized by a strong precipitation seasonality; 1200–1500 CE, with a gradual decrease in precipitation seasonality that accelerates at 1400 CE; and 1500–1950 CE, during which precipitation seasonality is the lowest (Fig. 6). After 1950 CE, most proxies display a return to increased precipitation seasonality, in agreement with recent trends observed in instrumental data from northern Chilean Patagonia (Appendix 3). Our interpretation of the PC29A sediment

455 record in terms of flood intensity and precipitation seasonality is further supported by (1)
456 the concomitant variations in accumulation rates, which reflect river sediment yield, and
457 sediment grain-size (Fig. 6), and (2) the increase in $\delta^{13}C$ values (Appendix 5) and the absence
458 of macroscopical organic remains, which both reflect weaker soil erosion, in the upper, i.e.,
459 less seasonal, part of the record.
460
461 5.3 Precipitation seasonality and the southern westerlies
462 The late Holocene changes in precipitation seasonality reconstructed from sediment core
463 PC29A can be interpreted in terms of latitudinal variations of the SWWB, using the modern
464 latitudinal distribution of precipitation seasonality over Chilean Patagonia (Fig. 1) as an
465 analog. The PC29A record displays high precipitation seasonality between 600 and 1200 CE.
466 Such a high seasonality likely reflects a more poleward position of the SWWB, resulting in a
467 precipitation regime around Quitralco fjord similar to the present-day conditions at 43–44ºS
468 (see Puerto Marin meteorological station in Fig. 1), i.e., a shift of the SSWB of ~2 degrees
469 compared to its present-day location. Following the same reasoning, the gradual decrease in
470 precipitation seasonality between 1200 and 1500 CE, followed by a very weak or no
471 seasonality in precipitation between 1500 and 1950 CE, is thought to represent a gradual
472 equatorward shift of the SWWB. This resulted in a precipitation regime in 1500–1950 CE
473 over Quitralco fjord similar to the present-day conditions found at 47–48ºS (see Isla San
474 Pedro meteorological station in Fig. 1). The return to slightly more seasonal precipitation
475 conditions during the last 50 years likely results from the recent poleward shift of the SWWB
476 (Shindell and Schmidt, 2004; Appendix 3). By comparison with modern precipitation regimes,
477 the amplitude of the latitudinal shift of the SWWB during the last 1400 years can be
478 estimated at about 3–4º of latitude. Although our precipitation seasonality reconstruction is

in good agreement with the recent increase in precipitation seasonality in northern Chilean Patagonia, it is in contradiction with the gridded reconstruction of Neukom et al. (2010), which shows that precipitation seasonality in Chilean Patagonia in 1931–1995 was lower than during any of the four previous centuries. This apparent discrepancy is mostly likely caused by the lack of records from the windward side of the Patagonian Andes in Neukom's reconstruction, which resulted in the over-extrapolation of records located at the lee-side of the Andes.

5.4 Comparison with other precipitation / SWWB records

The timing of the decrease in precipitation seasonality recorded in core PC29A at 1200–1500 CE roughly corresponds to a major reorganization of the climate system throughout the world, which is frequently associated to the Little Ice Age originally described in the Northern Hemisphere. Here, we compare the PC29A record to regional precipitation and SWWB reconstructions. We focus on records that (1) cover at least the same duration, and (2) reconstruct variability at multi-decadal to multi-centennial timescales. Although many tree-ring reconstructions exist in the region, these records were not included in our comparison since they only cover the last centuries and, most importantly, they are known to underestimate multi-centennial variability because of uncertainties in detrending (Esper et al., 2004; Marcott et al., 2013). In South-Central Chile (34–41ºS), several precipitation reconstructions show an increase in precipitation and therefore in westerly wind speed (cf Garreaud et al., 2013) during the last millennium (Fig. 7). The Lago Aculeo record, which is located close to the present-day northern limit of the SWWB in winter (34ºS) shows an increase in clastic layers, interpreted as representing increasing river floods in 1200–1800 CE (Jenny et al., 2002; Fig. 7a). Similarly, the pollen record of Laguna San Pedro (38ºS) reveals

503 an increase in the Nothofagus/Poaceae index, reflecting more humid conditions, between
504 1200 and 1850 CE (Fletcher and Moreno, 2012; Fig. 7b). Two records located at 40ºS display
505 a similar increase in precipitation of westerly origin during the 15th to 18th centuries. In
506 Puyehue lake, Bertrand et al. (2005) show increased accumulation rates of terrigenous
507 particles, interpreted as higher river discharge resulting from increased precipitation in
508 1470–1755 CE (Fig. 7c). Similarly, the marine sediment record GeoB3313-1 (41ºS) of Lamy et
509 al. (2001) provides evidence for increased precipitation at 1375–1750 CE, in addition to a
510 previous minor increase at 600–750 CE (Fig. 7d). A similar increase in precipitation of
511 westerly origin after 1200 CE was also interpreted from organic geochemical proxies in Jacaf
512 fjord sediments at 44ºS (Sepúlveda et al., 2009). Finally, the low resolution pollen record at
513 Alerce (41ºS) indicates high precipitation, and therefore strengthening of the westerlies,
514 between 1500 and 1850 CE (Heusser and Streeter, 1980). Together, these records provide
515 evidence for increased precipitation in south-central Chile (34–41ºS) starting in 1200–1500
516 CE and ending in 1750–1850 CE.
517 In southern Chilean Patagonia (> 50ºS), the pollen record of Lago Guanaco in Torres del
518 Paine (51ºS), reveals an increase in the Nothofagus/Poaceae index (NPI) between 1500 and
519 1900 CE (Fig. 7f), which, based on the present-day positive correlation between westerly
520 wind speed and precipitation at Torres del Paine, was originally interpreted as representing
521 stronger SWWB (Moreno et al., 2010). This interpretation was however challenged by Lamy
522 et al. (2010) and Kilian and Lamy (2012), who argue that because of the location of Torres
523 del Paine on the lee-side of the Andes, increases in the NPI index may actually represent
524 weaker westerly winds. The latter interpretation seems to be in agreement with the lake
525 level reconstruction of Laguna Potrok Aike. In this lake, which is located at 52ºS in
526 Argentinean Patagonia where precipitation is negatively correlated with westerly wind

strength, Habertzettl et al. (2005) identified a period of increased lake level, and therefore wetter conditions related to a decrease in the strength of the SWWB in 1460–1940 CE. Further south, the MA1 stalagmite record (53ºS) also provides evidence for a decrease in annual precipitation, and therefore a weakening of the westerlies, between 1400 CE and the present (Schimpf et al., 2011, Fig. 7g). Similarly, the sediment record from Lago Fagnano (Waldmann et al., 2010; Fig. 7h) suggests a decrease in precipitation of westerly origin, represented by a decrease in iron supply, in 1200–1850 CE. Although the Holocene lake and fjord sediment records of Lamy et al. (2010) cover the same region between 51 and 54ºS, these records do not show significant changes in precipitation during the last millennium, possibly due to their location in the core of the SWWB. Because of the constantly high wind speeds that occur in the core of the wind belt (50–55^{o}S; Fig. 2), small variations in the latitudinal position of the SWWB (i.e., 1–2 degrees), do likely not result in significant changes in precipitation at 51–54^{o}S. This makes this region relatively insensitive to low amplitude latitudinal shifts of the SWWB, despite the high and positive correlation between precipitation and westerly wind speed.

Although there is currently no straightforward record of Late Holocene westerly wind speed variations from the Antarctic Peninsula (e.g., Bentley et al., 2009), Koffman et al. (2013) used changes in the grain-size of dust particles in the WAIS Divide ice core to show that westerly wind speed at the southern boundary of the SWWB also decreased in 1400–1850 CE. Other Antarctic ice core records have been used to infer past changes in wind strength but these records are mostly based on the sea-salt sodium proxy, which is influenced by multiple parameters, such as atmospheric circulation and sea-ice cover, and can therefore not be unambiguously interpreted as variations in westerly wind speed (Koffman et al., 2013).

In summary, the interpretation of our Quitralco fjord sediment record in terms of latitudinal shifts of the SWWB during the last 1400 years is supported by most existing records from south-central and southern Chile. Low precipitation in south-central Chile (Fig. 7a–d) and high precipitation in southern Patagonia (Fig. 7 f–h) in 600–1000 CE agree with a southward position of the SSWB, as reflected in sediment core PC29A (Fig. 7e). Similarly, the northward shift of the SWWB that was identified from sediment core PC29A in 1200–1950 CE is supported by higher precipitation in south-central Chile in 1200–1800 CE (Lamy et al., 2001; Jenny et al., 2002; Bertrand et al., 2005; Fletcher and Moreno, 2012), lower precipitation at the southwestern tip of Patagonia in 1200–1850 CE (Moreno et al., 2010; Waldmann et al., 2010; Schimpf et al., 2011), and by the decrease in westerly wind speed over West Antarctica identified by Koffman et al. (2013). These records collectively provide evidence for a more southward location of the SWWB in 600–1000 CE, a northward shift in 1200–1500 CE and a sustained northward position in 1500–1900 CE. We cannot totally reject the hypothesis that the northward migration of the SWWB in 1200–1900 CE was accompanied by an expansion of the northern half of SWWB, which could explain the nearly simultaneous increase in precipitation over a large latitudinal range (e.g., 34º–41ºS). Contraction/expansion of the SWWB alone can however not explain the precipitation seasonality changes observed at site PC29A. To refine this interpretation and discuss the potential accompanying expansion/contraction of the SWWB, additional westerly wind speed records from the southern limit of the SWWB, i.e., the Antarctica Peninsula, are critically needed.

5.5 Comparison with sea surface temperature records

In the present-day environment, the seasonal contraction (expansion) of the SWWB in summer (winter) is associated with an increase (decrease) in SST gradient (Figs. 1, 2). This differs from glacial-interglacial timescales, for which models and paleoclimate reconstructions show that the SWWB migrated equatorward during glacials and shifted poleward during interglacials (Toggweiler et al., 2006; Kohfeld et al., 2013), although not all models agree (Sime et al., 2013). To assess the relation between changes in the latitudinal position of the SWWB and variations in SST during the late Holocene, we compare our PC29A precipitation seasonality record to existing SST records from the southeastern Pacific, Chilean fjord region and Antarctic Peninsula (Fig. 8).

The four existing SST records from the Patagonian region (41–51ºS; Fig. 8 a–d) display a consistent SST decrease of 1–1.5ºC during the last millennium, although the timing of the onset of the cooling trend varies among sites. It starts as early as 600 CE in core GeoB7186 (44ºS; Mohtadi et al., 2007), around 1150 CE in GeoB3313 (41ºS; Lamy et al., 2002) and PC33 (44ºS; Sepúveda et al., 2009), and around 1250 CE in MD07-3124 (51ºS; Caniupán et al., in press). These four records, which cover 10 degrees of latitude, all seem to point to a SST decrease of the southeastern Pacific that started between 600 and 1250 CE, and persisted until the last century. The relatively high variability of the SST at site PC33 (Jacaf Fjord, 44ºS) during the last 800 years is likely due to the episodic influence of cold river water input since this site is located in a narrow fjord with several river inflows.

Comparison between these SST records and the PC29A paleohydrology record (Fig. 8f) indicates that low precipitation seasonality in the Quitralco fjord area, and therefore equatorward-shifted SWWB, is coeval with low SSTs in the southeastern Pacific and vice versa. The relation between the amplitude of SST and SWWB changes over the last 1400 years (3–4º latitudinal shift of the SWWB and 1–1.5ºC SST decrease) is similar to the relation

597 that was suggested for glacial-interglacial timescales, during which the SWWB migrated over
598 7–10 degrees of latitude latitudinal and SSTs decreased by about 6ºC (Lamy et al., 2004;
599 Toggweiler et al., 2006). Our results therefore suggest that fluctuations in the latitudinal
600 position of the SWWB during the late Holocene are tightly linked to sea surface temperature
601 variability in the Southern Ocean and southeastern Pacific. The equatorward migration of
602 the SWWB that started in 1200 CE and peaked in 1500–1950 CE was clearly related to lower
603 SSTs in the Southern Ocean and southeastern Pacific.
604 For glacial-interglacial timescales, the modeling results of William et al. (2006) suggest the
605 following mechanism: large-scale SST decrease reduces convection in the tropics causing a
606 contraction of the Hadley cell, which in turn results in an equatorward shift of the SWWB.
607 Although SSTs also seem to decrease in the equatorial Pacific during the Late Holocene (Stott
608 et al., 2004), the amplitude of the cooling (<1ºC) seems too limited to cause a significant
609 decrease in the strength of the Hadley cell. Instead, we suggest that the equatorward
610 migration of the SWWB during the last millennium was caused by a strengthening of the
611 polar cell, as reflected by the strong (~5ºC) SST decrease around the Antarctic Peninsula (Fig.
612 8e; Shevenell et al., 2011). This hypothesis is supported by air temperature reconstructions
613 from continental Antarctica (e.g., Masson et al., 2000), which show a ~2ºC decrease between
614 ~1280 and 1900 CE (Bertler et al., 2011). The influence of air temperature on the latitudinal
615 position of the SWWB is further supported by the good agreement between variations in air
616 temperature in southern South America (PAGES 2k Consortium, 2013; Fig. 8g) and our
617 Quitralco fjord record, which show concomitant changes at multi-centennial to multi-
618 decadal timescales, with lower temperature being systematically associated with decreased
619 precipitation seasonality over Quitralco fjord, and therefore northward migration of the
620 SWWB. This relation is particularly striking for the 1725–1800 CE time-window (Fig. 8g),

during which higher air temperature is coeval with a southward migration of the SWWB, in agreement with the decrease in precipitation in nearby Lago Plomo (Elbert et al., 2011). The equatorward shift of the SWWB during the last millennium was very likely enhanced by increased sea-ice cover around Antarctica, as suggested by the sea-ice diatoms biomarker concentrations measured in ODP core 1098 (Etourneau et al., 2013), and by the sea-ice dependent $\delta^{18}O$ record of WAIS divide (Steig et al., 2013). In addition, the gradual equatorward migration of the SWWB likely caused the northward migration of the northern branch of the ACC, which reinforced the decrease of SSTs off Patagonia during the second half of the last millennium.

The mechanism proposed above differs from the seesaw-type redistribution of heat between the hemispheres that was invoked to explain the migration of the SWWB during the last deglaciation (Anderson et al., 2009; Toggweiler, 2009). This suggests that the SWWB may respond to different forcing mechanisms at different timescales. For the late Holocene, solar forcing may play an important role, as suggested by Varma et al. (2011). In addition, the early onset of cooling and migration of the SWWB in the Southern Hemisphere during the last millennium (1200 CE, or as early as 1000 CE according to some records, see Figs. 7 and 8) compared to the onset of changes in climate associated to the Little Ice Age in the Northern Hemisphere (1400 CE; Haug et al., 2001; Mann et al., 2009) suggests a forcing mechanism predominantly influencing the Southern Hemisphere.

6. Conclusions

Geochemical and sedimentological data obtained on sediment core PC29A (Quitralco fjord, 46ºS) were successfully used to reconstruct late Holocene changes in precipitation seasonality in the Andes of Northern Chilean Patagonia. Due to the distinct precipitation

regimes that exist immediately to the North (strong precipitation seasonality) and to the South (year-round precipitation) of Quitralco fjord, relatively small latitudinal shifts of the SWWB in either direction result in large changes in precipitation seasonality. Our paleohydrological reconstruction can therefore be directly interpreted in terms of latitudinal shifts of the SWWB, reconciling most previously-published late Holocene records of SWWB variability in Patagonia. Our sediment record suggests a poleward-shifted SWWB between 600 and 1200 CE, followed by a gradual shift towards the equator between 1200 and 1500 CE, and stabilization in a sustained equatorward position between 1500 and 1950 CE. The most recent part of the record displays a return to a slightly poleward shifted SWWB, in agreement with recent trends observed in climatological data. Comparison with SST reconstructions off Chilean Patagonia shows a tight link between latitudinal variations of the SWWB and SSTs during the late Holocene, with the SWWB being systematically shifted poleward when SSTs are higher and vice versa. This pattern resembles the variability that occurs at glacial-interglacial timescales. We suggest that late Holocene variations in the SWWB are driven by changes in the strength of the polar cell, which responds to temperature variations at the high latitudes of the Southern Hemisphere. By comparison, tropical climate probably had little influence on the SWWB during the late Holocene. Finally, the early onset of SST decrease and SWWB equatorward migration compared to the Northern Hemisphere Little Ice Age suggests that the forcing mechanism predominantly influences the Southern Hemisphere. Extending our precipitation seasonality record to the entire Holocene would very likely solve the discrepancies that currently exist regarding the evolution of the SWWB during the Holocene.

Acknowledgments

We acknowledge the Chilean National Oceanographic Committee (CONA) for financial support to carry out the Cimar-7 Fiordo Program (Grant C7F 01-10 to Silvio Pantoja). The captain and crew of the AGOR Vidal Gormaz are thanked for their professional support during the expedition. Liviu Giosan and Jess Tierney (WHOI) are acknowledged for their help with the ITRAX XRF core scanner. We are grateful to Maureen Auro, Joanne Goudreau and Olivier Rouxel (WHOI) for making possible the geochemical measurements by FAAS, to Steve Manganini (WHOI) for providing access to the coulometer, to Jan-Berend Stuut and Inka Meyer (MARUM, Bremen, Germany) for sharing the Coulter grain size analyzer and running the end-member algorithm, to Nathalie Fagel (ULg, Belgium) for providing access to the x-ray diffractometer, and to Marco Coolen and Edward Sholkovitz (WHOI) for supplying some of the material used for sample preparation. The Chilean Dirección General de Aguas (DGA) and the Servicio Hidrográfico y Oceanográfico de la Armada (SHOA) provided the meteorological data presented in figure 1a and appendix 3. We acknowledge the authors of data presented in figures 7 and 8 for making their results available. This research was supported by a BAEF fellowship (Belgian American Educational Foundation) and an EU FP6 Marie Curie Outgoing Fellowship to S. Bertrand. J. Sepúlveda was supported by Fundación Andes through the WHOI/University of Concepción agreement, and by a scholarship from the Graduate School of the University of Concepción. S. Bertrand is currently a postdoctoral fellow of the Flemish Research Foundation (Belgium). Two anonymous reviewers provided detailed and constructive comments on an earlier version of this paper. The dataset presented in this article is available on PANGAEA: http://doi.pangaea.de/10.1594/PANGAEA.829370

References

692 Anderson, R.F., Ali, S., Bradtmiller, L.I., Nielsen, S.H.H., Fleisher, M.Q., Anderson, B.E., Burckle, L.H.,
693 2009. Wind-Driven Upwelling in the Southern Ocean and the Deglacial Rise in Atmospheric CO2.
694 Science 323, 1443–1448.
695 Aravena, J.C., Luckman, B.H., 2009. Spatio-temporal rainfall patterns in Southern South America.
696 International Journal of Climatology 29, 2106–2120.
697 Araya-Vergara, J.F., 1997. Geomorphological profiles of the fjords and longitudinal depression of
698 North-Patagonia. Ciencia y Tecnología del Mar 20, 3–22.
699 Bentley, M.J., Hodgson, D.A., Smith, J.A., Cofaigh, C.O., Domack, E.W., Larter, R.D., Roberts, S.J.,
700 Brachfeld, S., Leventer, A., Hjort, C., Hillenbrand, C.D., Evans, J., 2009. Mechanisms of Holocene
701 palaeoenvironmental change in the Antarctic Peninsula region. Holocene 19, 51–69.
702 Bertler, N.A.N., Mayewski, P.A., Carter, L., 2011. Cold conditions in Antarctica during the Little Ice Age
703 - Implications for abrupt climate change mechanisms. Earth Planet Sc Lett 308, 41–51.
704 Bertrand, S., Boës, X., Castiaux, J., Charlet, F., Urrutia, R., Espinoza, C., Lepoint, G., Charlier, B., Fagel,
705 N., 2005. Temporal evolution of sediment supply in Lago Puyehue (Southern Chile) during the last
706 600 yr and its climatic significance. Quaternary Res 64, 163–175.
707 Bertrand, S., Hughen, K.A., Lamy, F., Stuut, J.B.W., Torrejón, F., Lange, C.B., 2012a. Precipitation as
708 the main driver of Neoglacial fluctuations of Gualas glacier, Northern Patagonian Icefield. Clim
709 Past 8, 519–534.
710 Bertrand, S., Hughen, K.A., Sepúlveda, J., Pantoja, S., 2012b. Geochemistry of surface sediments from
711 the fjords of Northern Chilean Patagonia (44–47ºS): Spatial variability and implications for
712 paleoclimate reconstructions. Geochimica Et Cosmochimica Acta 76, 125–146.
713 Blaauw, M., 2010. Methods and code for 'classical' age-modelling of radiocarbon sequences.
714 Quaternary Geochronology 5, 512–518.
715 Boex, J., Fogwill, C., Harrison, S., Glasser, N.F., Hein, A., Schnabel, C., Xu, S., 2013. Rapid thinning of
716 the late Pleistocene Patagonian Ice Sheet followed migration of the Southern Westerlies.
717 Scientific Reports 3.

718 Brindley, G.W., Brown, G., 1980. Crystal structures of clay minerals and their X-ray identification.
719 Mineralogical Society of London, UK.
720 Campbell, C., 1998. Late Holocene lake sedimentology and climate change in southern Alberta,
721 Canada. Quaternary Res 49, 96–101.
722 Caniupán, M., Lamy, F., Lange, C.B., Kaiser, J., Kilian, R., Arz, H.W., León, T., Mollenhauer, G.,
723 Sandoval, S., De Pol-Holz, R., Pantoja, S., Wellner, J., Tiedemann, R., in press. Holocene sea-
724 surface temperature variability in the Chilean fjord region. Quaternary Res. DOI:
725 10.1016/j.yqres.2014.07.009
726 Carter, S.J., Colman, S.M., 1994. Biogenic Silica in Lake Baikal Sediments - Results from 1990–1992
727 American Cores. J Great Lakes Res 20, 751-760.
728 Cook, H.E., Johnson, P.D., Matti, J.C., Zemmels, I., 1975. Methods of sample preparation and X-ray
729 diffraction data analysis, X-ray Mineralogy Laboratory, Deep Sea Drilling Project, University of
730 California, Riverside, In: Hayes, D.E., Frakes, L.A., al., e. (Eds.), Initial Reports of the Deep Sea
731 Drilling Project, Washington (U.S. Govt. Printing Office), pp. 999–1007.
732 Elbert, J., Grosjean, M., von Gunten, L., Urrutia, R., Fischer, D., Wartenburger, R., Ariztegui, D., Fujak,
733 M., Hamann, Y., 2011. Quantitative high-resolution winter (JJA) precipitation reconstruction from
734 varved sediments of Lago Plomo 47^{o}S, Patagonian Andes, AD 1530-2002. The Holocene 22, 465-
735 474.
736 Esper, J., Frank, D.C., Wilson, R.J.S., 2004. Climate reconstructions: Low-frequency ambition and high-
737 frequency ratification. Eos, Transactions American Geophysical Union 85, 113-120.
738 Etourneau, J., Collins, L.G., Willmott, V., Kim, J.H., Barbara, L., Leventer, A., Schouten, S., Damste,
739 J.S.S., Bianchini, A., Klein, V., Crosta, X., Masse, G., 2013. Holocene climate variations in the
740 western Antarctic Peninsula: evidence for sea ice extent predominantly controlled by changes in
741 insolation and ENSO variability. Clim Past 9, 1431–1446.

742 Fletcher, M.S., Moreno, P.I., 2012. Vegetation, climate and fire regime changes in the Andean region
743 of southern Chile (38ºS) covaried with centennial-scale climate anomalies in the tropical Pacific
744 over the last 1500 years. Quaternary Sci Rev 46, 46–56.
745 Garreaud, R., Lopez, P., Minvielle, M., Rojas, M., 2013. Large-Scale Control on the Patagonian
746 Climate. J Climate 26, 215–230.
747 Giguet-Covex, C., Arnaud, F., Enters, D., Poulenard, J., Millet, L., Francus, P., David, F., Rey, P.J.,
748 Wilhelm, B., Delannoy, J.J., 2012. Frequency and intensity of high-altitude floods over the last 3.5
749 ka in northwestern French Alps (Lake Anterne). Quaternary Res 77, 12–22.
750 Grangeon, T., Legout, C., Esteves, M., Gratiot, N., Navratil, O., 2012. Variability of the particle size of
751 suspended sediment during highly concentrated flood events in a small mountainous catchment.
752 J Soil Sediment 12, 1549–1558.
753 Guerra, A.J.T., Soares Da Silva, A., 2011. Predicting soil loss and runoff from forest roads and seasonal
754 cropping systems in Brazil using WEPP, In: Morgan, R.P.C., Nearing, M.A. (Eds.), Handbook of
755 erosion modelling. Wiley-Blackwell, Chichester, West Sussex, UK ; Hoboken, NJ, pp. 186–194.
756 Gut, B., 2008. Trees in patagonia, Basel.
757 Haberzettl, T., Fey, M., Lucke, A., Maidana, N., Mayr, C., Ohlendorf, C., Schabitz, F., Schleser, G.H.,
758 Wille, M., Zolitschka, B., 2005. Climatically induced lake level changes during the last two
759 millennia as reflected in sediments of Laguna Potrok Aike, southern Patagonia (Santa Cruz,
760 Argentina). J Paleolimnol 33, 283–302.
761 Haug, G.H., Hughen, K.A., Sigman, D.M., Peterson, L.C., Rohl, U., 2001. Southward migration of the
762 intertropical convergence zone through the Holocene. Science 293, 1304–1308.
763 Heusser, C.J., Streeter, S.S., 1980. A Temperature and Precipitation Record of the Past 16,000 Years in
764 Southern Chile. Science 210, 1345–1347.
765 Hijmans, R.J., Cameron, S.E., Parra, J.L., Jones, P.G., Jarvis, A., 2005. Very high resolution interpolated
766 climate surfaces for global land areas. International Journal of Climatology 25, 1965–1978.

767 Hogg, A.G., Hua, Q., Blackwell, P.G., Niu, M., Buck, C.E., Guilderson, T.P., Heaton, T.J., Palmer, J.G.,
768 Reimer, P.J., Reimer, R.W., Turney, C.S.M., Zimmerman, S.R.H., 2013. SHCal13 Southern
769 Hemisphere Calibration, 0–50,000 years cal BP. Radiocarbon 55, 1889–1903.
770 Hooke, R.L., 2000. Toward a uniform theory of clastic sediment yield in fluvial systems. Geol Soc Am
771 Bull 112, 1778–1786.
772 Huang, S.L., Sholkovitz, E.R., Conte, M.H., 2007. Application of high-temperature fusion for analysis of
773 major and trace elements in marine sediment trap samples. Limnol Oceanogr-Meth 5, 13–22.
774 Jenny, B., Valero-Garcés, B.L., Urrutia, R., Kelts, K., Veit, H., Appleby, P.G., Geyh, M., 2002. Moisture
775 changes and fluctuations of the Westerlies in Mediterranean Central Chile during the last 2000
776 years: The Laguna Aculeo record (33º50'S). Quatern Int 87, 3–18.
777 Kaufman, C.A., Lamoureux, S.F., Kaufman, D.S., 2011. Long-term river discharge and multidecadal
778 climate variability inferred from varved sediments, southwest Alaska. Quaternary Res 76, 1–9.
779 Kilian, R., Lamy, F., 2012. A review of Glacial and Holocene paleoclimate records from southernmost
780 Patagonia (49–55ºS). Quaternary Sci Rev 53, 1–23.
781 Koffman, B.G., Kreutz, K.J., Breton, D.J., Kane, E.J., Winski, D.A., Birkel, S.D., Kurbatov, A.V., Handley,
782 M.J., 2013. Centennial-scale shifts in the position of the Southern Hemisphere westerly wind belt
783 over the past millennium. Clim. Past Discuss. 9, 3125–3174.
784 Kohfeld, K.E., Graham, R.M., de Boer, A.M., Sime, L.C., Wolff, E.W., Le Quéré, C., Bopp, L., 2013.
785 Southern Hemisphere westerly wind changes during the Last Glacial Maximum: paleo-data
786 synthesis. Quaternary Sci Rev 68, 76-95.
787 Lamy, F., Gersonde, R., Winckler, G., Esper, O., Jaeschke, A., Kuhn, G., Ullermann, J., Martinez-Garcia,
788 A., Lambert, F., Kilian, R., 2014. Increased dust deposition in the Pacific Southern Ocean during
789 glacial periods. Science 343, 403-407.Lamy, F., Hebbeln, D., Rohl, U., Wefer, G., 2001. Holocene
790 rainfall variability in southern Chile: a marine record of latitudinal shifts of the Southern
791 Westerlies. Earth Planet Sc Lett 185, 369–382.

792 Lamy, F., Kaiser, J., Ninnemann, U., Hebbeln, D., Arz, H.W., Stoner, J., 2004. Antarctic timing of
793 surface water changes off Chile and Patagonian ice sheet response. Science 304, 1959–1962.
794 Lamy, F., Kilian, R., Arz, H.W., Francois, J.P., Kaiser, J., Prange, M., Steinke, T., 2010. Holocene changes
795 in the position and intensity of the southern westerly wind belt. Nature Geoscience 3, 695–699.
796 Lamy, F., Ruhlemann, C., Hebbeln, D., Wefer, G., 2002. High- and low-latitude climate control on the
797 position of the southern Peru-Chile Current during the Holocene. Paleoceanography 17.
798 Lenzi, M.A., Marchi, L., 2000. Suspended sediment load during floods in a small stream of the
799 Dolomites (northeastern Italy). Catena 39, 267–282.
800 Luebert, F., Pliscoff, P., 2006. Sinopsis bioclimática y vegetacional de Chile, 1st ed. Editorial
801 Universitaria, Santiago de Chile.
802 Mann, M.E., Zhang, Z.H., Rutherford, S., Bradley, R.S., Hughes, M.K., Shindell, D., Ammann, C.,
803 Faluvegi, G., Ni, F.B., 2009. Global Signatures and Dynamical Origins of the Little Ice Age and
804 Medieval Climate Anomaly. Science 326, 1256–1260.
805 Marcott, S.A., Shakun, J.D., Clark, P.U., Mix, A.C., 2013. A reconstruction of regional and global
806 temperature for the past 11,300 years. Science 339, 1198-1201.
807 Masiokas, M.H., Villalba, R., Luckman, B.H., Lascano, M.E., Delgado, S., Stepanek, P., 2008. 20th-
808 century glacier recession and regional hydroclimatic changes in northwestern Patagonia. Global
809 Planet Change 60, 85–100.
810 Masson, V., Vimeux, F., Jouzel, J., Morgan, V., Delmotte, M., Ciais, P., Hammer, C., Johnsen, S.,
811 Lipenkov, V.Y., Mosley-Thompson, E., Petit, J.R., Steig, E.J., Stievenard, M., Vaikmae, R., 2000.
812 Holocene climate variability in Antarctica based on 11 ice-core isotopic records. Quaternary Res
813 54, 348–358.
814 Mayewski, P.A., Meredith, M.P., Summerhayes, C.P., Turner, J., Worby, A., Barrett, P.J., Casassa, G.,
815 Bertler, N.A.N., Bracegirdle, T., Garabato, A.C.N., Bromwich, D., Campbell, H., Hamilton, G.S.,
816 Lyons, W.B., Maasch, K.A., Aoki, S., Xiao, C., van Ommen, T., 2009. State of the Antarctic and
817 Southern Ocean Climate System. Rev Geophys 47.

818 Meehl, G.A., Stocker, T.F., Collins, W.D., Friedlingstein, P., Gaye, A.T., Gregory, J.M., Kitoh, A., Knutti,
819 R., Murphy, J.M., Noda, A., Raper, S.C.B., Watterson, I.G., Weaver, A.J., Zhao, Z.-C., 2007. Global
820 Climate Projections, In: Solomon, S., Qin, D., Manning, M., Chen, Z., Marquis, M., Averyt, K.B.,
821 Tignor, M., H.L., M. (Eds.), Climate Change 2007: The Physical Science Basis. Contribution of
822 Working Group I to the Fourth Assessment Report of the Intergovernmental Panel on Climate
823 Change Cambridge University Press, Cambridge, United Kingdom and New York, NY, USA.
824 Meza, F.J., 2013. Recent trends and ENSO influence on droughts in Northern Chile: An application of
825 the Standardized Precipitation Evapotranspiration Index. Weather and Climate Extremes 1, 51–
826 58.
827 Miller, A., 1976. The climate of Chile, In: Schwerdtfeger, W. (Ed.), Climates of Central and South
828 America. Elsevier Scientific Pub. Co., Amsterdam ; New York, pp. 107–134.
829 Milliman, J.D., 1997. Fluvial sediment discharge to the sea and the importance of regional tectonics,
830 In: Ruddiman, W.F. (Ed.), Tectonic uplift and climate change. Plenum Press, New York, pp. 239–
831 257.
832 Minetti, J.L., Vargas, W.M., Poblete, A.G., Acuna, L.R., Casagrande, G., 2003. Non-linear trends and
833 low frequency oscillations in annual precipitation over Argentina and Chile, 1931-1999.
834 Atmosfera 16, 119-135.
835 Mohtadi, M., Romero, O.E., Kaiser, J., Hebbeln, D., 2007. Cooling of the southern high latitudes
836 during the Medieval Period and its effect on ENSO. Quaternary Sci Rev 26, 1055–1066.
837 Moreno, P.I., Francois, J.P., Moy, C.M., Villa-Martinez, R., 2010. Covariability of the Southern
838 Westerlies and atmospheric CO2 during the Holocene. Geology 38, 727–730.
839 Moreno, P.I., Francois, J.P., Villa-Martinez, R.P., Moy, C.M., 2009. Millennial-scale variability in
840 Southern Hemisphere westerly wind activity over the last 5000 years in SW Patagonia.
841 Quaternary Sci Rev 28, 25–38.
842 Moreno, P.I., Vilanova, I., Villa-Martinez, R., Garreaud, R.D., Rojas, M., De Pol-Holz, R., 2014.
843 Southern Annular Mode-like changes in southwestern Patagonia at centennial timescales over the

844 last three millennia. Nature communications 5, 4375.Mortlock, R.A., Froelich, P.N., 1989. A Simple
845 Method for the Rapid-Determination of Biogenic Opal in Pelagic Marine-Sediments. Deep-Sea Res 36,
846 1415–1426.
847 Murray, R., Miller, D., Kryc, K., 2000. Analysis of major and trace elements in rocks, sediments, and
848 interstitial waters by inductively coupled plasma–atomic emission spectrometry (ICP-AES), ODP
849 Technical Note, pp. 1–27.
850 Naranjo, J.A., Stern, C.R., 1998. Holocene explosive activity of Hudson Volcano, southern Andes. B
851 Volcanol 59, 291–306.
852 Neukom, R., Luterbacher, J., Villalba, R., Kuttel, M., Frank, D., Jones, P.D., Grosjean, M., Esper, J.,
853 Lopez, L., Wanner, H., 2010. Multi-centennial summer and winter precipitation variability in
854 southern South America. Geophys Res Lett 37.
855 Noren, A.J., Bierman, P.R., Steig, E.J., Lini, A., Southon, J., 2002. Millennial-scale storminess variability
856 in the northeastern United States during the Holocene epoch. Nature 419, 821–824.
857 PAGES 2k consortium, 2013. Continental-scale temperature variability during the past two millennia.
858 Nature Geoscience 6, 339–346.
859 Pankhurst, R.J., Weaver, S.D., Herve, F., Larrondo, P., 1999. Mesozoic-Cenozoic evolution of the
860 North Patagonian Batholith in Aysen, southern Chile. J Geol Soc London 156, 673–694.
861 Parris, A.S., Bierman, P.R., Noren, A.J., Prins, M.A., Lini, A., 2010. Holocene paleostorms identified by
862 particle size signatures in lake sediments from the northeastern United States. J Paleolimnol 43,
863 29–49.
864 Quintana, J., Aceituno, P., 2006. Trends and interdecadal variability of rainfall in Chile, 8th ICSHMO,
865 Foz do Iguaçu, Brazil, pp. 371–372.
866 Quintana, J.M., Aceituno, P., 2012. Changes in the rainfall regime along the extratropical west coast
867 of South America (Chile): 30–43ºS. Atmosfera 25, 1–22.
868 Reid, I., Frostick, L.E., 1994. Fluvial sediment transport and deposition, In: Pye, K. (Ed.), Sediment
869 transport and depositional processes. Blackwell Scientific Publications, Oxford, pp. 89–155.

870 Salinas, C.X., Mendieta, J., 2013. Mitigation and adaptation investments for desertification and
871 climate change: an assessment of the socioeconomic return. Mitig Adapt Strat Gl 18, 659–672.
872 Schimpf, D., Kilian, R., Kronz, A., Simon, K., Spotl, C., Worner, G., Deininger, M., Mangini, A., 2011.
873 The significance of chemical, isotopic, and detrital components in three coeval stalagmites from
874 the superhumid southernmost Andes (53ºS) as high-resolution palaeo-climate proxies.
875 Quaternary Sci Rev 30, 443–459.
876 Sepúlveda, J., Pantoja, S., Hughen, K.A., Bertrand, S., Figueroa, D., León, T., Drenzek, N.J., Lange, C.,
877 2009. Late Holocene sea-surface temperature and precipitation variability in northern Patagonia,
878 Chile (Jacaf Fjord, 44ºS). Quaternary Res 72, 400–409.
879 Sernageomin, 2003. Mapa geologico de Chile version digital, escala 1/1.000.000.
880 Shevenell, A.E., Ingalls, A.E., Domack, E.W., Kelly, C., 2011. Holocene Southern Ocean surface
881 temperature variability west of the Antarctic Peninsula. Nature 470, 250–254.
882 Shindell, D.T., Schmidt, G.A., 2004. Southern Hemisphere climate response to ozone changes and
883 greenhouse gas increases. Geophys Res Lett 31.
884 SHOA, 2004. Canales Erraruiz, Costa y Estero Elefantes, bathymetric map 1/70.000.
885 Sievers, H.A., Silva, N., 2008. Water masses and circulation in austral Chilean channels and fjords, In:
886 Silva, N., Palma, S. (Eds.), Progress in the oceanographic knowledge of Chilean interior waters,
887 from Puerto Montt to Cape Horn. Comité Oceanográfico Nacional–Pontificia Universidad Católica
888 de Valparaíso, Valparaiso, Chile, pp. 53–58.
889 Silva, N., Guzmán, D., 2006. Condiciones oceanográficas físicas y químicas, entre boca del guafo y
890 fiordo aysén (crucero cimar 7 fiordos). Ciencia y Tecnología del Mar 29, 25–44.
891 Sime, L.C., Kohfeld, K.E., Le Quéré, C., Wolff, E.W., de Boer, A.M., Graham, R.M., Bopp, L., 2013.
892 Southern Hemisphere westerly wind changes during the Last Glacial Maximum: model-data
893 comparison. Quaternary Sci Rev 64, 104-120.
894 Steig, E.J., Ding, Q.H., White, J.W.C., Kuttel, M., Rupper, S.B., Neumann, T.A., Neff, P.D., Gallant,
895 A.J.E., Mayewski, P.A., Taylor, K.C., Hoffmann, G., Dixon, D.A., Schoenemann, S.W., Markle, B.R.,

Fudge, T.J., Schneider, D.P., Schauer, A.J., Teel, R.P., Vaughn, B.H., Burgener, L., Williams, J., Korotkikh, E., 2013. Recent climate and ice-sheet changes in West Antarctica compared with the past 2,000 years. Nature Geoscience 6, 372–375.

Stern, C.R., Moreno, H., Lopez-Escobar, L., Clavero, J.E., Lara, L.E., Naranjo, J.A., Parada, M.A., Skewes, M.A., 2007. Chilean Volcanoes, In: Moreno, T., Gibbons, W. (Eds.), The geology of Chile. Geological Society of London, London, pp. 147–178.

Stott, L., Cannariato, K., Thunell, R., Haug, G.H., Koutavas, A., Lund, S., 2004. Decline of surface temperature and salinity in the western tropical Pacific Ocean in the Holocene epoch. Nature 431, 56–59.

Strub, P.T., Mesias, J.M., Montecino, V., Ruttlant, J., Salinas, S., 1998. Coastal ocean circulation off western South America, In: Robinson, A.R., Brink, K.H. (Eds.), The Sea. Wiley, New York, pp. 273–315.

Thompson, D.W.J., Solomon, S., Kushner, P.J., England, M.H., Grise, K.M., Karoly, D.J., 2011. Signatures of the Antarctic ozone hole in Southern Hemisphere surface climate change. Nature Geoscience 4, 741–749.

Toggweiler, J.R., 2009. Shifting Westerlies. Science 323, 1434–1435.

Toggweiler, J.R., Russell, J.L., Carson, S.R., 2006. Midlatitude westerlies, atmospheric CO2, and climate change during the ice ages. Paleoceanography 21.

Vandekerkhove, E., 2014. The volcanic ash soils of Northern Chilean Patagonia (44°– 48°S): Distribution, weathering and influence on river chemistry. MSc thesis, Ghent University, Belgium, 72 p.Varma, V., Prange, M., Lamy, F., Merkel, U., Schulz, M., 2011. Solar-forced shifts of the Southern Hemisphere Westerlies during the Holocene. Clim Past 7, 339–347.

Vera, C., Silvestri, G., Liebmann, B., Gonzalez, P., 2006. Climate change scenarios for seasonal precipitation in South America from IPCC-AR4 models. Geophys Res Lett 33.

Verardo, D.J., Froelich, P.N., Mcintyre, A., 1990. Determination of Organic–Carbon and Nitrogen in Marine-Sediments Using the Carlo-Erba-Na-1500 Analyzer. Deep-Sea Res 37, 157–165.

922 Vieira, R., 2002. Morfogénesis y dinámica de las vertientes submarinas en la costa de fiordos de
923 Norpatagonia, Chile. MSc thesis, Universidad de Chile, Santiago, 101 p.
924 Villa-Martínez, R., Moreno, P.I., 2007. Pollen evidence for variations in the southern margin of the
925 westerly winds in SW Patagonia over the last 12,600 years. Quaternary Res 68, 400–409.
926 Waldmann, N., Ariztegui, D., Anselmetti, F.S., Austin, J.A., Moy, C.M., Stern, C., Recasens, C., Dunbar,
927 R.B., 2010. Holocene climatic fluctuations and positioning of the Southern Hemisphere westerlies
928 in Tierra del Fuego (54ºS), Patagonia. J Quaternary Sci 25, 1063–1075.
929 Waldmann, N., Borromei, A.M., Recasens, C., Olivera, D., Martínez, M.A., Maidana, N.I., Ariztegui, D.,
930 Austin Jr., J.A., Anselmetti, F.S., 2014. Integrated reconstruction of Holocene millennial-scale
931 environmental changes in Tierra del Fuego, southernmost South America. Palaeogeography,
932 Palaeoclimatology, Palaeoecology 399, 294–309.
933 Walling, D.E., Moorehead, P.W., 1989. The Particle-Size Characteristics of Fluvial Suspended
934 Sediment - an Overview. Hydrobiologia 176, 125–149.
935 Walling, D.E., Owens, P.N., Waterfall, B.D., Leeks, G.J.L., Wass, P.D., 2000. The particle size
936 characteristics of fluvial suspended sediment in the Humber and Tweed catchments, UK. Sci Total
937 Environ 251, 205–222.
938 Warren, C.R., 1993. Rapid Recent Fluctuations of the Calving San-Rafael Glacier, Chilean Patagonia -
939 Climatic or Non-Climatic. Geogr Ann A 75, 111–125.
940 Weltje, G.J., Prins, M.A., 2007. Genetically meaningful decomposition of grain-size distributions.
941 Sediment Geol 202, 409–424.
942 Wingenter, O.W., Elliott, S.M., Blake, D.R., 2010. New Directions: Restoring the westerly winds in the
943 Southern Hemisphere: Climate's lever. Atmospheric Environment 44, 3866–3868.
944

Core depth (cm)	Laboratory code	Material	^{14}C (yr BP±1σ)	2 σ calibrated age range (min–max, yr CE)
17.25	OS-38281	Mollusk	890±35	1478–1643
75	OS-38282	Mollusk	1290±30	1229–1381

92.25	OS-38359	Plant/Wood	910±30	1048–1260
142	OS-38360	Plant/Wood	1280±30	685–881
185.5	OS-53093	Plant/Wood	1400±30	636–764
199.5	OS-53339	Plant/Wood	1510±35	540–647
205.5	OS-38305	Plant/Wood	1430±75	521–857

945

946 **Table 1** – Radiocarbon ages obtained on sediment core PC29A. The ages were calibrated
947 with CLAM 2.2 (Blaauw, 2010), using the calibration curve SHCal13 (Hogg et al., 2013). A
948 reservoir correction of 530 years was applied to the two mollusk samples.

949

950 **Figure captions**

951

952 **Figure 1** – Modern hydroclimatology (1950–2000) and oceanography (1981–2010) of
953 southern South America. (a) Annual mean precipitation and annual mean sea surface
954 temperature. Monthly precipitation (1980–2010) data are represented for meteorological
955 stations located near coring site PC29A (Puerto Chacabuco), as well as two degrees of
956 latitude to the North (Puerto Marin) and to the South (Isla San Pedro). The seasonality index
957 (value under monthly precipitation charts) was calculated as the ratio between winter and
958 summer precipitation (JJA/DJF). Values higher (lower) than 1 are therefore indicative of
959 regions where precipitation is higher (lower) in winter than in summer. Note that the Puerto
960 Marin precipitation record only starts in 1993. The major ocean currents are schematically
961 represented according to Strub et al. (1998) (ACC: Antarctic Circumpolar Current; CFW:
962 Chilean Fjord Water). (b) Austral winter (JJA) and summer (DJF) precipitation and sea surface
963 temperature, and difference between the two (seasonality). The precipitation maps were
964 created using data from the worldclim database (Hijmans et al., 2005), and the SST data are
965 from the NOAA Extended Reconstructed Sea Surface Temperature (SST) V3b
966 (http://www.esrl.noaa.gov/psd/data/gridded/data.noaa.ersst.html). See appendix 1 for the
967 animated map.

968

969 **Figure 2** – Present-day climatology (1981–2010) of the Southern Hemisphere. Austral
970 summer (a) and winter (b) wind speed and direction at 850 hPa (NCEP/NCAR reanalysis). The
971 color scale represents only the zonal component of wind velocity. The same color scale was
972 used for both figures to facilitate the comparison between summer and winter wind

patterns. (c) Annual cycles of 850 hPa zonal wind zonally averaged over the eastern Pacific (75º – 90ºW) in the Southern Hemisphere (0–80ºS).

Figure 3 – Watershed (white line) of Rio Pelu represented on a natural color landsat image (LandsatLook) taken on February 11, 2011. The coring site in Quitralco fjord (PC29A) is represented by a red dot.

Figure 4 – Composition of sediment core PC29A. The four sediment components are expressed in weight percent of dry sediment. Error bars correspond to 1 sigma.

Figure 5 – CLAM age model of sediment core PC29A. The grey levels represent the density of probability (bayesian age-depth modeling).

Figure 6 – Selected geochemical (Fe and Ti XRF core scanner intensities, Fe/Al, Ti/Al and litho-si/Al), mineralogical (quartz content) and grain-size (arithmetic mean) proxies in sediment core PC29A. The sediment accumulation rates were computed from the age model presented in Fig. 5.

Figure 7 – Selected paleoclimate and paleoenvironmental records from the Southern Hemisphere and comparison with the PC29A paleoprecipitation record. (a) Magnetic susceptibility of Laguna Aculeo (Jenny et al., 2002). High MS values represent flood layers. (b) Nothofagus/Poaceae index of Laguna San Pedro (Fletcher and Moreno, 2012). The green line corresponds to the 50-yr running average. (c) Highest accumulation rates of terrigenous particles in Lago Puyehue (Bertrand et al., 2005). (d) High precipitation periods derived from

997 the iron content of sediment core GeoB3313-3 (Lamy et al., 2001). (e) Fe/Al of core PC29A
998 (this study). (f) Lago Guanaco Nothofagus/Poaceae index (Moreno et al., 2010). (g) Yttrium
999 concentration in stalagmite MA1 (Schimpf et al., 2011). (h) Iron content in Lago Fagnano
1000 (Waldmann et al., 2010). Iron values corresponding to turbidites were removed from the
1001 dataset. The core chronology is from Waldmann et al. (2014). The records are presented
1002 from North to South, and all proxies are plotted such as wind strength increases towards the
1003 top of the figure. See section 5.4 for interpretation of the individual records.
1004
1005 **Figure 8** – Comparison between the PC29A precipitation seasonality reconstruction and
1006 temperature records from the southeastern Pacific, Patagonian fjords, and Antarctic
1007 Peninsula. The sea surface temperature (SST) records are organized with increasing latitude
1008 from top to bottom: (a) GeoB3313 (Lamy et al., 2002), (b) GeoB7186 (Mohtadi et al., 2007),
1009 (c) PC33 (Jacaf fjord; Sepúveda et al., 2009), (d) MD07-3124 (Canal Concepción; Caniupán et
1010 al., in press), (e) ODP 1098 (Shevenell et al., 2011). (f) PC29A precipitation seasonality
1011 reconstruction (this work). (g) Reconstruction of air temperature for South America (30-year
1012 standardized mean; PAGES 2k consortium, 2013). Warmer colors represent warmer air
1013 temperature and vice versa, as in the original article.
1014
1015

Appendix captions

Appendix 1 – Seasonal variability of precipitation in southern South America. The precipitation data is from the worldclim database (Hijmans et al., 2005). The red star represents coring site PC29A.

Appendix 2 – Correlation between monthly precipitation at Puerto Chacabuco (45.5°S; 60 km to the NE of coring site PC29A) and zonal wind speed at 700 hPa (1965–2012). The white star represents coring site PC29A.

Appendix 3 – Recent (1980–2010) trends in annual (a–f), summer [DJF] (g–l), and winter [JJA] (m–r) precipitation, and in the precipitation seasonality index [JJA/DJF] (s–x), for 6 meteorological stations on the western coast of northern Chilean Patagonia (41–48ºS). The 30-yr trends in precipitation (a–r) are indicated in absolute (mm/yr) and relative (difference between 2010 and 1980, in %) values. On the precipitation seasonality plots (s–x), the relative trends between 2010 and 1980 (in %) are indicated, as well as the average value of the index for the 1980–2010 period. Stations Marin Balmaceda (43.8ºS) and Puerto Aysen (45.4ºS) were not included because of a lack of data before 1994, and between 1979 and 1992, respectively. All stations show a marked increase in precipitation seasonality between 1980 and 2010, which varies between 3.5% and 40.0% (average 18.8%). Graphs y-af represent the trends in the same variables but for longer timescales, for the two stations that best represent our study area (Puerto Aysen and Puerto Chacabuco). Data source: Dirección General de Aguas (DGA, Chile), except for Faro San Pedro (Servicio Hidrográfico y Oceanográfico de la Armada [SHOA], Chile).

1040

1041 **Appendix 4** – Differences in seasonal precipitation between the 21st and 20th century
1042 according to the Coupled Model Intercomparison Project phase 3 (CMIP3) dataset. Maps
1043 were created using the IPCC Interactive mapping website of the Center for Climatic Research
1044 (CCR) at the University of Wisconsin-Madison
1045 (http://ccr.aos.wisc.edu/resources/data_scripts/ipcc_maps/). The white circle indicates the
1046 location of Quitralco fjord.

1047

1048 **Appendix 5** – Bulk organic geochemical data obtained on gravity core PC29A and on box
1049 core BC29A. The fraction of terrestrial carbon was calculated from the $\delta^{13}C$ data, using end-
1050 member values of -19.86‰ and -27.72‰ (Bertrand et al., 2012b) for the marine and
1051 terrestrial end-members, respectively.

1052

1053 **Appendix 6** – Particle size and end-member modeling results for core PC29A.
1054 (a) Grain-size of sediment core PC29A versus age. Two modes of grain sizes are apparent.
1055 The fine mode corresponds to fine silt grains (2–12 µm) and the coarser mode is composed
1056 of coarse silt (20–63 µm). The dominating mode is coarse between 600 and 1450 CE, and
1057 fine between 1450 CE and the top of the record.
1058 (b) Average (dashed line), minimum and maximum (grey area) particle size frequency
1059 distribution for the entire dataset (n = 52).
1060 (c) Seasonal floods (EM1) and background sedimentation (EM2) end-members from the two
1061 end-member model. The two end-member model explains 67% of the variance of the total
1062 set of grain-size distributions.
1063 (d) EM1 scores versus depth.

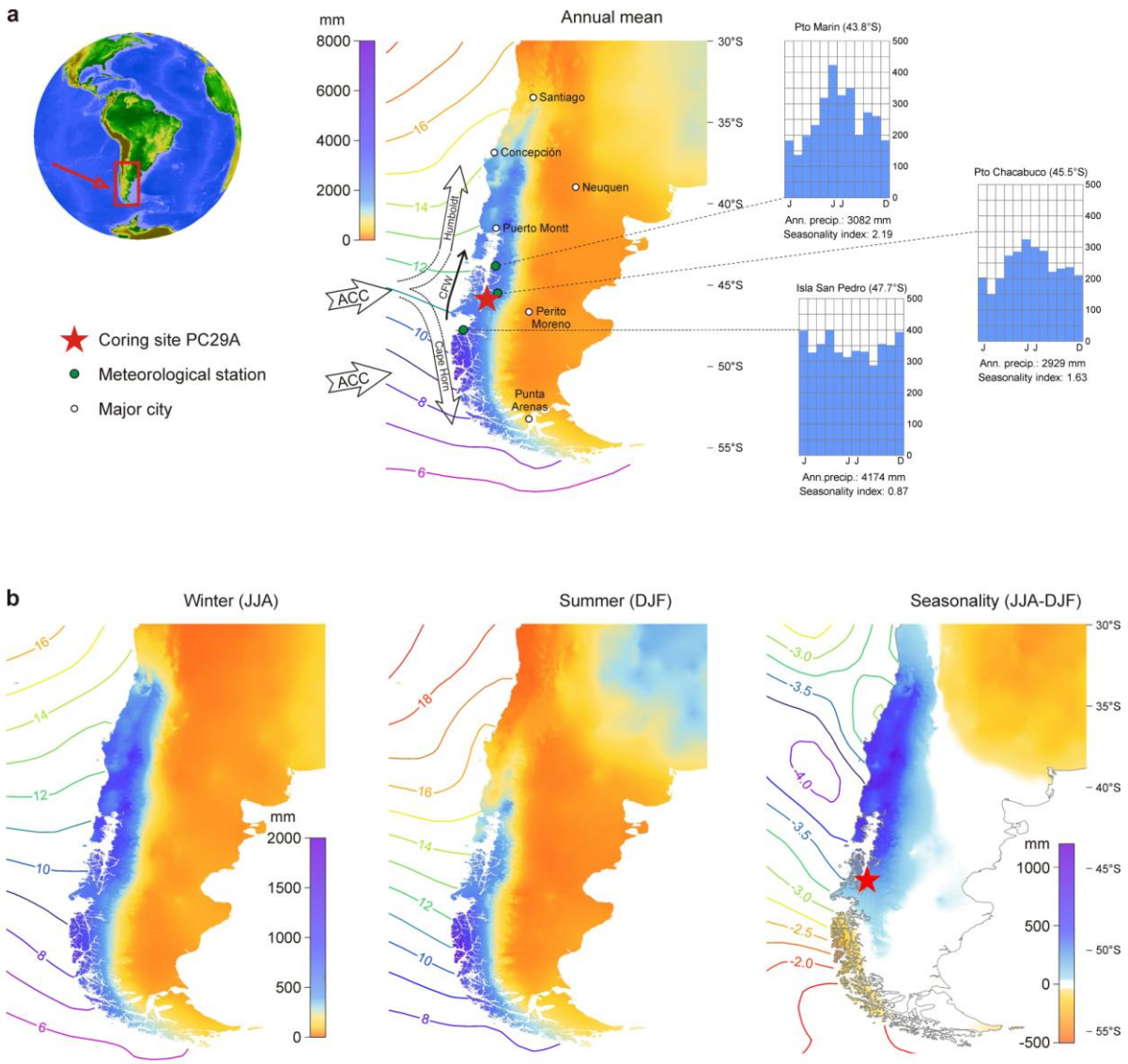
a
Annual mean
mm
8000
6000
4000
2000
0
Coring site PC29A
Meteorological station
Major city
Santiago
Concepción
Neuquen
Puerto Montt
Perito Moreno
Punta Arenas
Humboldt
CPFW
Cape Horn
ACC
ACC
30°S
35°S
40°S
45°S
50°S
55°S
Pto Marin (43.8°S)
Ann. precip.: 3082 mm
Seasonality index: 2.19
Isla San Pedro (47.7°S)
Ann.precip.: 4174 mm
Seasonality index: 0.87
Pto Chacabuco (45.5°S)
Ann. precip.: 2929 mm
Seasonality index: 1.63
b
Winter (JJA)
Summer (DJF)
Seasonality (JJA-DJF)
mm
2000
1500
1000
500
0
1000
500
0
-500

Figure 1

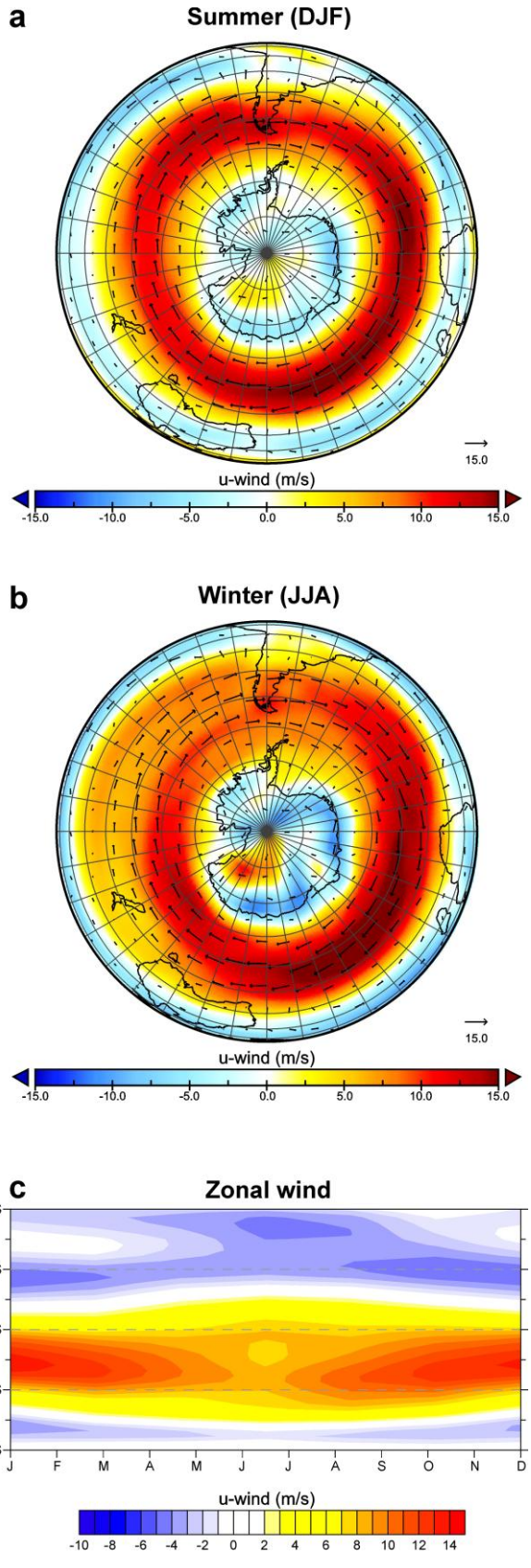
a
Summer (DJF)
15.0
u-wind (m/s)
-15.0 -10.0 -5.0 0.0 5.0 10.0 15.0
b
Winter (JJA)
15.0
u-wind (m/s)
-15.0 -10.0 -5.0 0.0 5.0 10.0 15.0
c
Zonal wind
0°S
20°S
40°S
60°S
80°S
J F M A M J J A S O N D
u-wind (m/s)
-10 -8 -6 -4 -2 0 2 4 6 8 10 12 14

Figure 2

1069

1070 Figure 3

1071

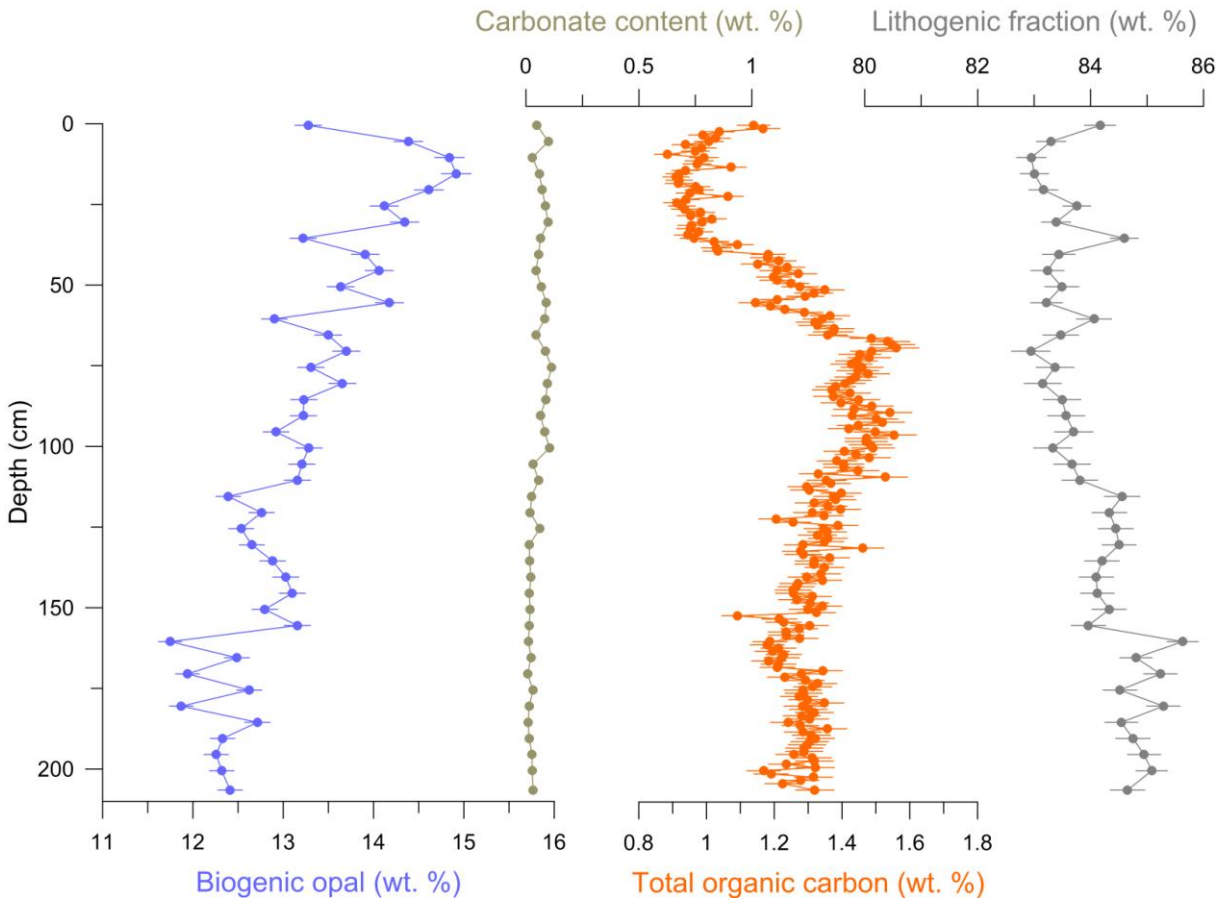

1072

1073 Figure 4

1074

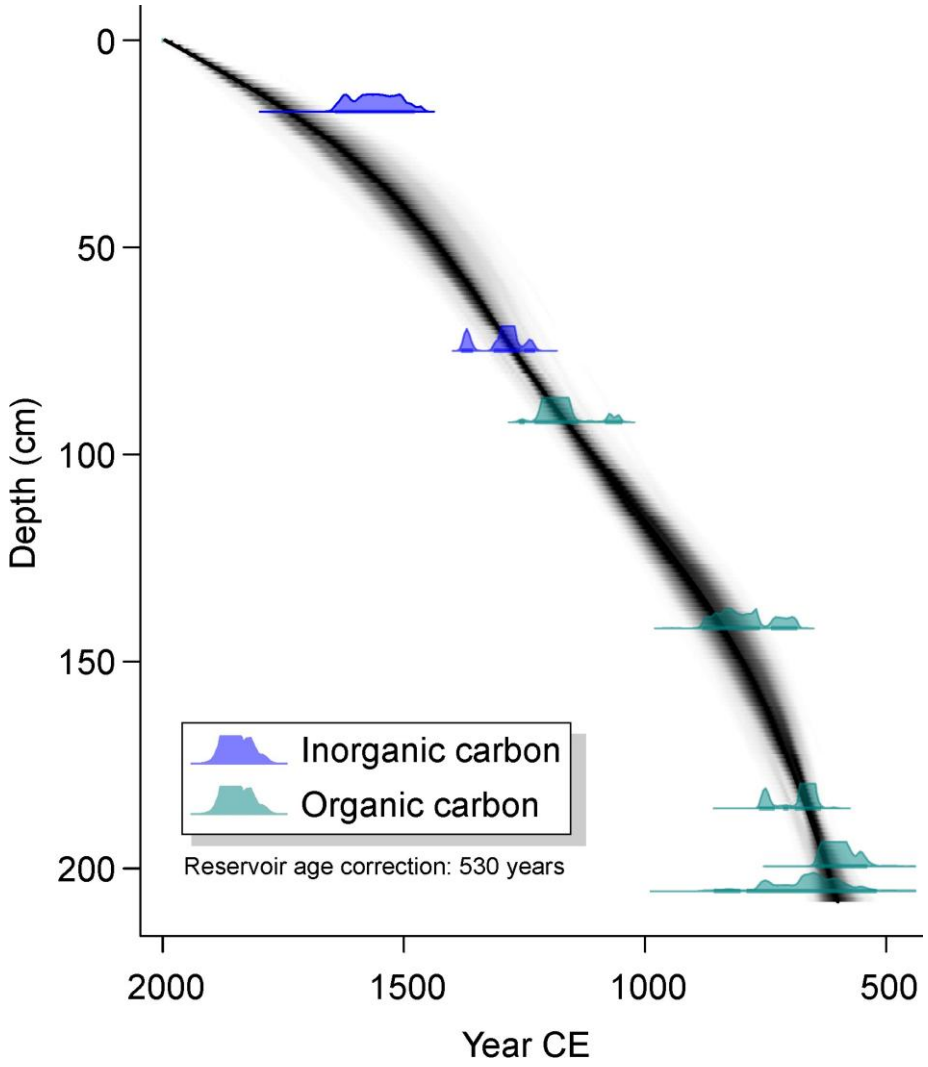
0
50
100
150
200
Depth (cm)
2000
1500
1000
500
Year CE
Inorganic carbon
Organic carbon
Reservoir age correction: 530 years

Figure 5

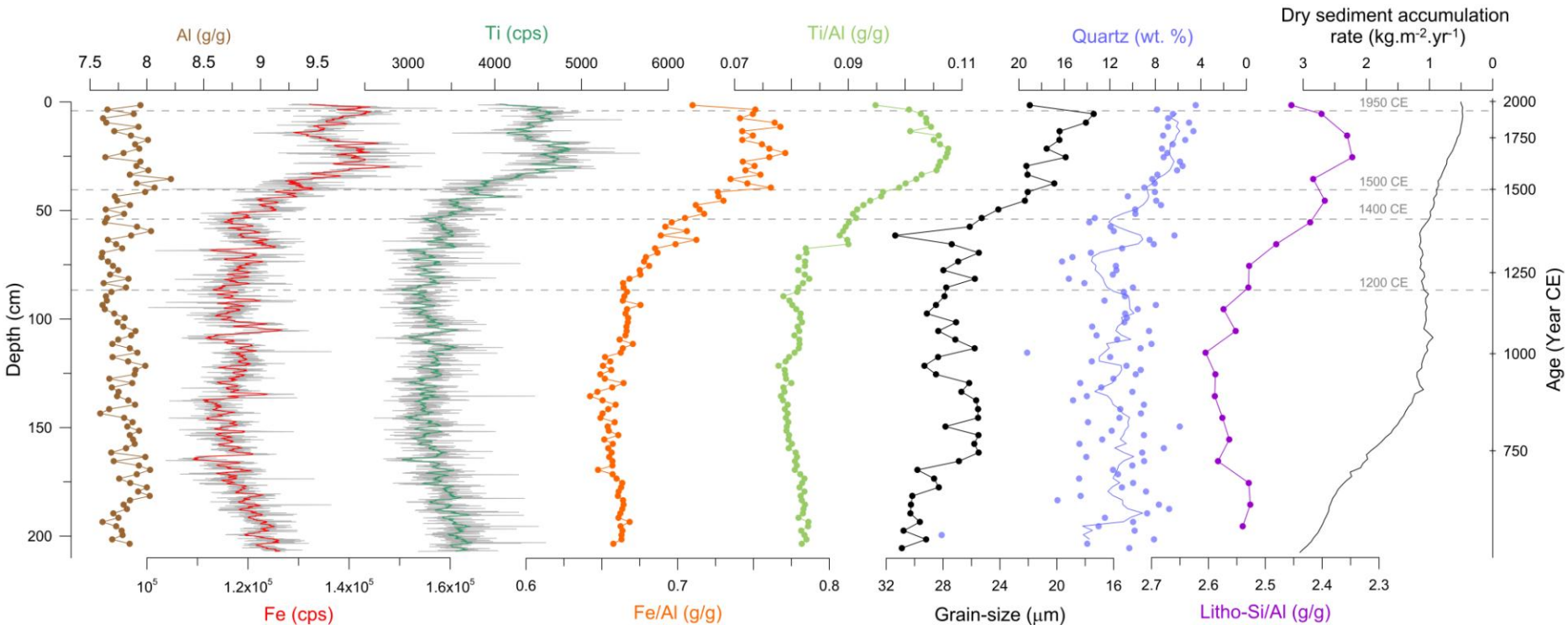
Al (g/g)
Ti (cps)
Ti/Al (g/g)
Quartz (wt. %)
Dry sediment accumulation rate (kg.m-2.yr-1)
Depth (cm)
Age (Year CE)
1950 CE
1500 CE
1400 CE
1200 CE
Fe (cps)
Fe/Al (g/g)
Grain-size (µm)
Litho-Si/Al (g/g)

Figure 6

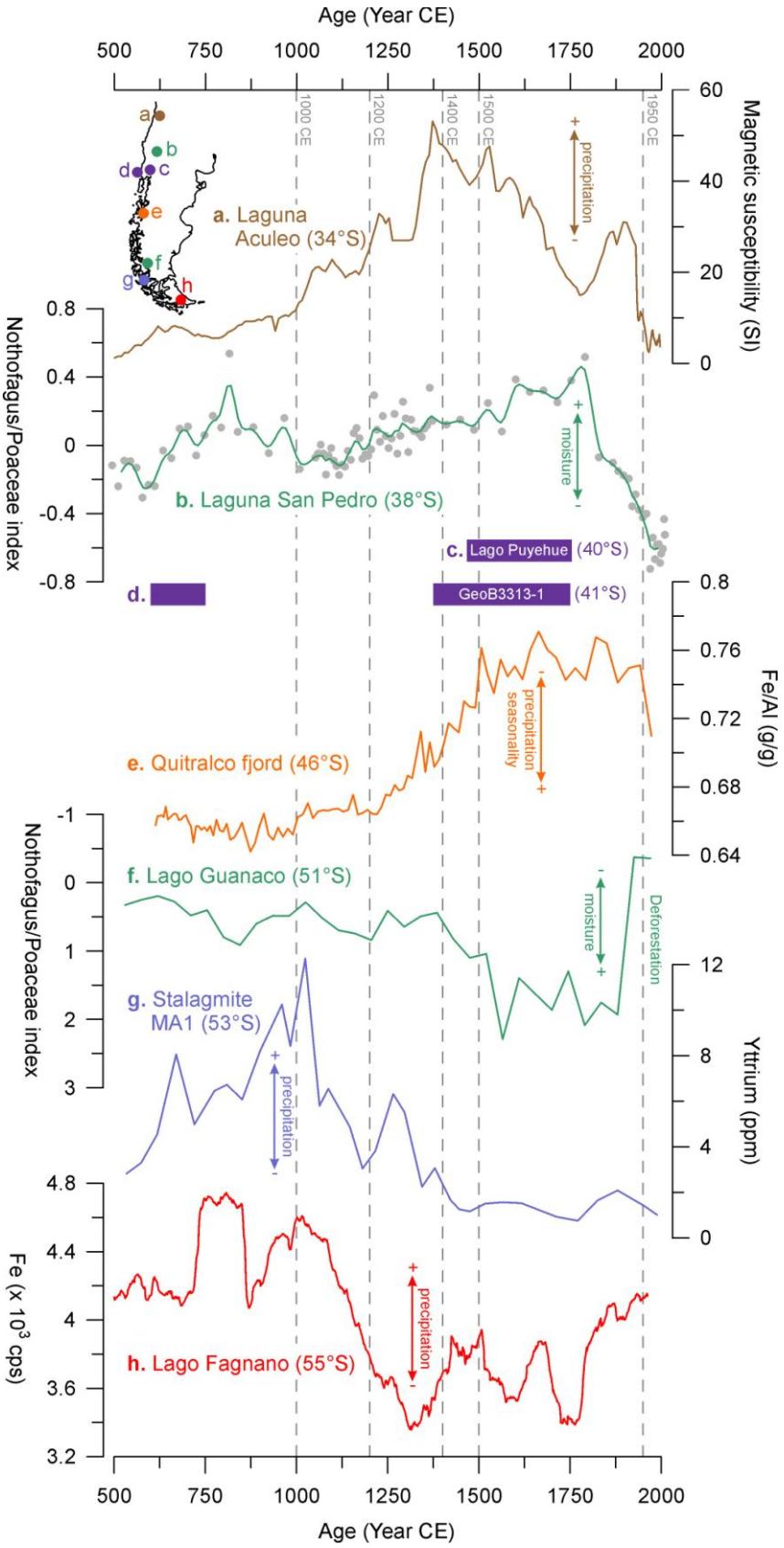
Age (Year CE)
500
750
1000
1250
1500
1750
2000
1000 CE
1200 CE
1400 CE
1500 CE
1950 CE
a
b
c
d
e
f
g
h
a. Laguna Aculeo (34°S)
precipitation
Magnetic susceptibility (SI)
60
40
20
0
Nothofagus/Poaceae index
0.8
0.4
0
-0.4
-0.8
b. Laguna San Pedro (38°S)
moisture
c. Lago Puyehue (40°S)
d.
GeoB3313-1 (41°S)
e. Quitralco fjord (46°S)
precipitation seasonality
Fe/Al (g/g)
0.8
0.76
0.72
0.68
0.64
f. Lago Guanaco (51°S)
moisture
Deforestation
-1
0
1
2
3
g. Stalagmite MA1 (53°S)
precipitation
12
8
4
0
Yttrium (ppm)
h. Lago Fagnano (55°S)
precipitation
Fe (x 10³ cps)
4.8
4.4
4
3.6
3.2
500
750
1000
1250
1500
1750
2000
Age (Year CE)

Figure 7

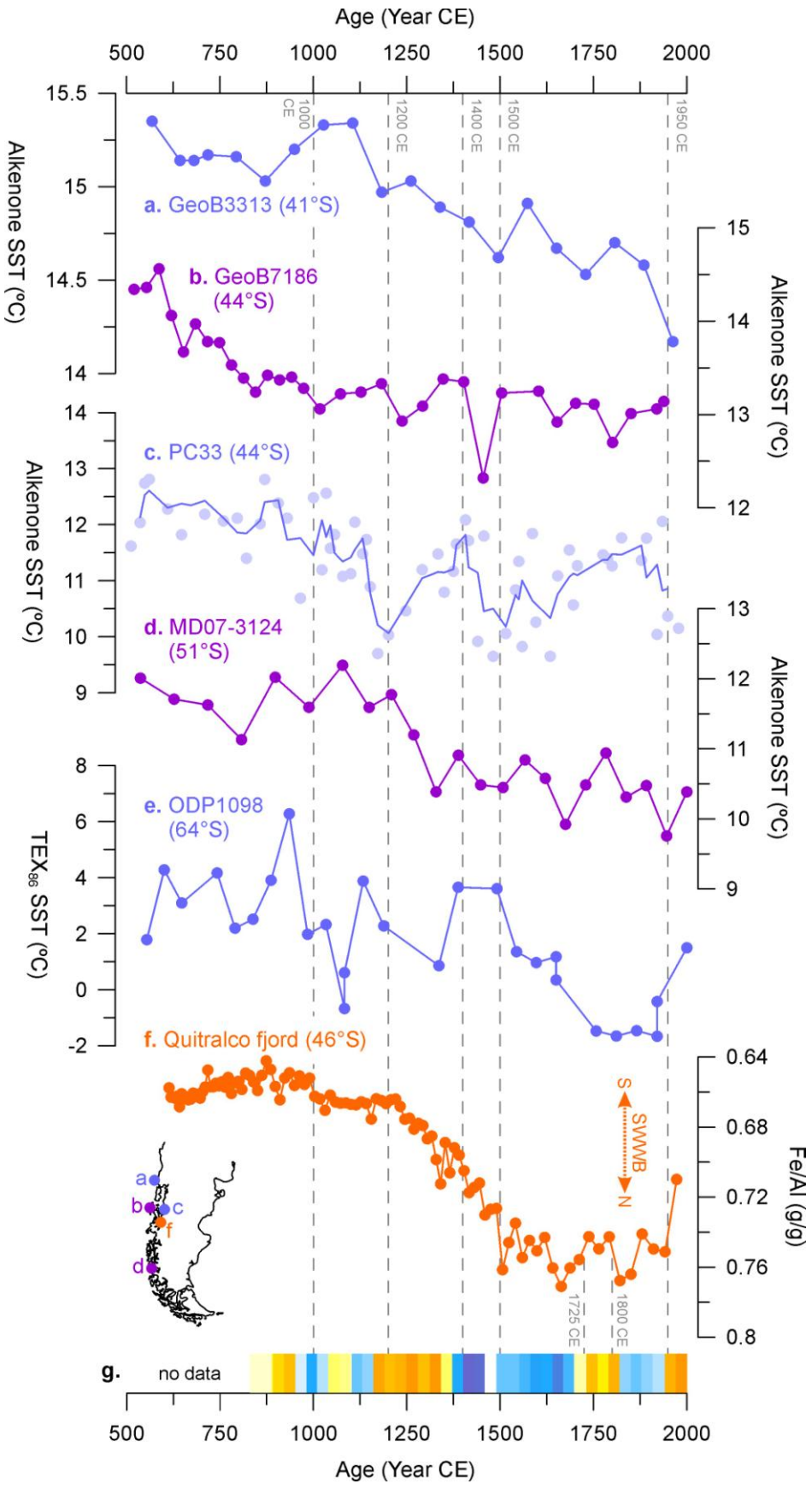

1083

1084 Figure 8